
Article:
Byrd, E.J., Crossley, J.A., Chau, C.C.C. et al. (Accepted: 2026) An ALS-Associated Mutation in the C-terminal α-helix of TDP-43 Uncouples Condensate Formation and Amyloid Assembly. Protein Science. ISSN: 0961-8368 (In Press)

An ALS-Associated Mutation in the C-terminal α-helix of TDP-43 Uncouples Condensate Formation and Amyloid Assembly

Emily J. Byrd[1], Joel A. Crossley[1], Chalmers C. C. Chau[2,3], Paolo Actis[2,3], Antonio N. Calabrese[1*]

[1]Astbury Centre for Structural Molecular Biology, School of Molecular and Cellular Biology, Faculty of Biological Sciences, University of Leeds, Leeds, LS2 9JT, UK.

[2]School of Electronic and Electrical Engineering, University of Leeds, LS2 9JT, UK.

[3]Bragg Centre for Materials Research, University of Leeds, LS2 9JT, UK.

* To whom correspondence should be addressed: A.Calabrese@leeds.ac.uk

ABSTRACT

TAR DNA-binding protein 43 (TDP-43) plays a critical role in RNA metabolism and is incorporated into biomolecular condensates called stress granules. In amyotrophic lateral sclerosis (ALS) and several other neurodegenerative disorders, TDP-43 undergoes aberrant phase transitions, forming insoluble amyloid aggregates, including fibrils composed of solely its intrinsically disordered C-terminal domain (CTD). Despite its central role in disease, the conformational dynamics of the CTD remain poorly understood due to its heterogeneous and transient conformational landscape. Here, we employ native ion mobility - mass spectrometry (IM-MS) using nanopipette sub-micron nano electrospray ionisation (nanoESI) emitters to characterise the conformational landscape of wild-type (WT) and ALS-associated TDP-43 CTD variants (Q331K and R361S) under different solution conditions. Our data suggest that mutations and salt concentration modulate the CTD's conformations. Combined with Thioflavin T fluorescence, light scattering, and microscopy we reveal that these conformational shifts correlate with altered amyloid assembly kinetics and propensity to form condensates. Notably, the Q331K variant, which has a mutation in the transient α-helical region in the CTD, has reduced propensity to form biomolecular condensates but can undergo amyloid assembly in the absence of condensate formation, suggesting that sequence alterations in this α-helical region can tune the molecular mechanism of amyloid assembly. This study demonstrates the power of IM-MS in probing disordered proteins and reveals mechanistic insights into how disease-associated mutations differentially tune TDP-43 CTD amyloid assembly mechanisms.

INTRODUCTION

TAR DNA-binding protein 43 (TDP-43) is an RNA-binding protein that plays a central role in the regulation of RNA splicing, stability, transport, and translation[1,2]. It is predominantly localised in the nucleus under basal conditions, but in response to cellular stress TDP-43 migrates to the cytoplasm where it contributes to the formation of biomolecular condensates known as stress granules [3,4]. Condensate formation is a dynamic and reversible process that facilitates sub-organellar compartmentalisation[5–8]. While TDP-43 condensate formation is believed to be part of a normal cellular stress response, aberrations in this process are implicated in neurodegenerative diseases, suggesting a switch from function to dysfunction[8–10]. TDP-43 is composed of 414 amino acids, comprising a structured N-terminal domain followed by two RNA recognition motifs (RRMs), RRM1 and RRM2, which are connected by unstructured linkers (Figure 1a)[11–13]. The C-terminal domain (CTD) is primarily intrinsically disordered and referred to as a low complexity domain (LCD) as it comprises primarily glycine and aromatic residues, as well as a distribution of proline residues known to promote condensate formation[14], and it also lacks charged residues (Figure 1b-e)[15]. The CTD is also thought to be a key driver of TDP-43 condensate formation (Figure 1f), and it features a small, transient α-helix (CTH; Figure 1b,g) which has been shown to undergo allosteric changes in dynamics upon RNA binding to RRM1 and RRM2[16,17].

In pathological contexts, TDP-43 undergoes irreversible liquid-to-solid transitions, forming insoluble cytoplasmic amyloid fibrils that are a defining hallmark of amyotrophic lateral sclerosis (ALS) and other TDP-43 proteinopathies[18]. These aggregates consist of full-length TDP-43 as well as truncated fragments comprising the C-terminal region (the proteins are often hyperphosphorylated and ubiquitinated[19]). A range of C-terminal fragments (CTFs) have been identified, including CTF-16 which comprises the CTD in isolation (studied here), CTF-25, a 25 kDa fragment comprising the CTD and part of RRM2, and a less frequently observed CTF-35 which comprises the CTD, RRM2, RRM1 and part of the NTD[20,21]. Fibril structures of both full-length TDP-43 and truncations comprising the entire C-terminal domain *in vitro* (CTD; residues ~267-414)[13] have been determined using cryogenic electron microscopy (cryo-EM)[22–26]. Structures of TDP-43 amyloid fibrils isolated from the frontal and motor cortices of ALS and frontotemporal lobar degeneration (FTLD) patients have revealed distinct fibril polymorphs[24,27], suggesting that specific amyloid folds are characteristic of different TDP-43 proteinopathies. Recently, the structure of filaments from individuals with FTLD (type C) were determined and shown to be comprised of heteromeric amyloid filaments composed of TDP-43 as well as a second protein ANXA11, a calcium-dependent phospholipid binding protein[25,28]. Amyloid fibrils formed *in vitro* from the entire CTD of TDP-43 revealed fibrils formed from a single protofilament comprised of a large 139-residue amyloid core[23]. Additionally, TDP-43 is known to undergo many

different post translational modifications (PTMs) such as acetylation, SUMOylation, ubiquitination, methylation, citrullination and phosphorylation which likely influence the function and dysfunction of the protein[29–36].

Notably, the intrinsically disordered CTD of TDP-43 is critical for both condensate formation and pathological amyloid assembly[16,37–39]. The CTD is enriched in glycine and aromatic residues (Figure 1c), harbours most of the known disease-associated mutations, and is prone to amyloid formation[1,31,37,40–42]. The conformational flexibility of the CTD presents a major challenge for structural characterisation, especially under physiological conditions. Nuclear magnetic resonance (NMR) spectroscopy has been applied to characterise the transient CTH in the monomeric TDP-43 CTD and shown that the CTH (residues 320-343) becomes stabilised in dimeric assemblies[43]. Additionally, G335 and G338 were identified as "helix terminators" and when mutated to alanine this results in enhanced condensate assembly, suggesting that helix enhancing mutations tune the TDP-43 CTD's ability to form biomolecular condensates[16]. Amyloid assembly of the TDP-43 CTD is known to proceed through condensate-mediated or hydrogel-mediated assembly[44]. The addition of salt has been shown to promote TDP-43 CTD condensate assembly by enhancing intermolecular contacts through electrostatic screening (including the protein backbone and termini as there are only three negatively charged residues in the CTD; Figure 1b) biasing the TDP-43 CTD towards condensate-driven amyloid assembly[39,44].

By contrast with the averaging which occurs in NMR spectroscopy experiments, native ion mobility–mass spectrometry (IM-MS) offers the ability to resolve distinct conformational states based on their rotationally averaged collision cross section (CCS), enabling the interrogation of heterogeneity within a conformational ensemble *in vacuo* with high sensitivity[45–48]. Proteins are ionised using nano electrospray ionisation (nanoESI) under non-denaturing conditions and kinetically trapped in their solution phase states, typically using a solution comprising volatile salts such as ammonium acetate to facilitate transfer into the gas phase[49,50]. Under standard nanoESI conditions, salts such as Na^+, K^+, PO_4^{3-} can cause ion suppression and adduct to protein ions, which reduces spectral resolution and sensitivity[51–54]. We, and others[54–59], have recently demonstrated the use of submicron nanoESI "nanopipette" emitters[54–58] which enable nanoESI analysis in biochemical buffers and under elevated salt concentrations.

Here, we use submicron nanoESI emitters to investigate the effect of increasing ionic strength on the CCS distributions of the TDP-43 CTD and two ALS-associated TDP-43 CTD variants (Q331K and R361S) as measured by travelling wave IM-MS in nitrogen gas ($^{TW}CCS_{N2}$), to elucidate how solution conditions tune the structural properties of the monomeric TDP-43 CTD. The Q331K mutation lies within a region

98 that adopts α-helical structure (Figure 1a), whereas the R361S mutation is present outside of the α-
99 helix[60,61]. These two variants enabled us to understand how modulating the structured CTH element
100 within the otherwise low sequence complexity CTD tunes the structural and functional properties of
101 TDP-43 CTD. In combination with nanopipette nanoESI emitters we interrogated the role of NaCl in
102 tuning TDP-43 CTD conformations. To contextualise the conformational changes observed via IM-MS,
103 we complimented our mass spectrometry data with multiple orthogonal biophysical assays. We
104 employed Thioflavin T (ThT) fluorescence assays to monitor amyloid assembly kinetics, while light
105 scattering (nephelometry) and differential interference contrast (DIC) microscopy provided insights
106 into condensate formation. Our results reveal that elevated salt concentrations induce measurable
107 shifts in the CTD conformational ensemble, as reflected by changes in its CCS distributions. These
108 conformational shifts correlate with increased amyloidogenicity for Q331K TDP-43 CTD. The Q331K
109 mutation, present within the C-terminal α-helix, reduces the propensity for condensate formation
110 under the conditions tested, but this variant can still form amyloid fibrils under elevated salt
111 concentrations in the absence of condensates. These findings highlight the role of electrostatic
112 interactions in modulating the balance between condensate formation and pathological amyloid
113 assembly and demonstrates how a single amino acid substitution can tune the self-assembly
114 mechanism of TDP-43. Taken together, our results highlight the critical role of the CTH region in
115 governing the route of amyloid assembly for the TDP-43 CTD and demonstrate how a single mutation
116 in this region can alter the mechanism of amyloid assembly.

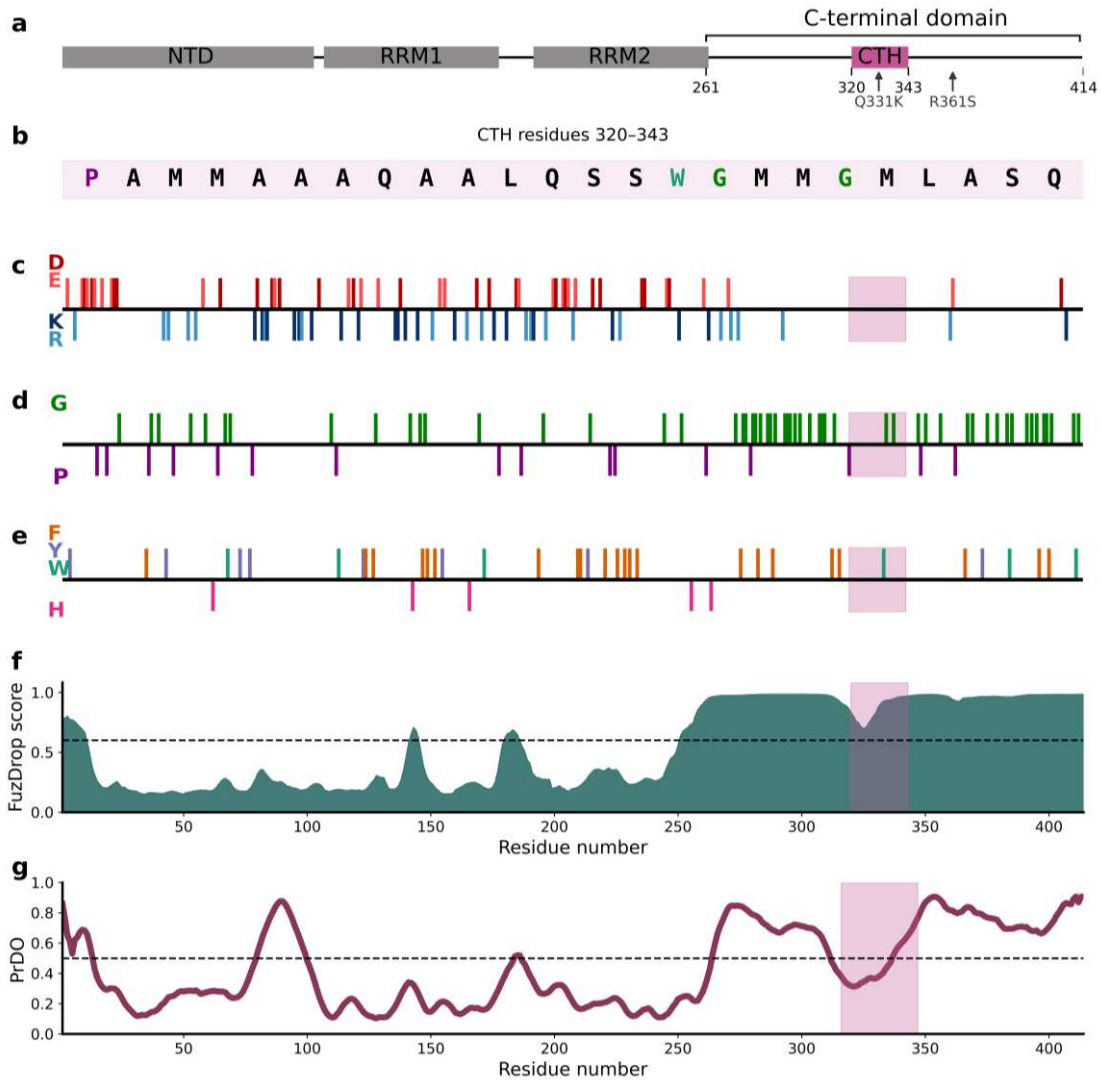

Figure 1 Bioinformatic analysis of the TDP-43 protein sequence. *(a) Schematic of the domain architecture of TDP-43, showing the N-terminal domain (NTD), RNA recognition motifs (RRM1 and RRM2) and the intrinsically disordered CTD. The CTH is highlighted in pink and the location of the Q331K and R361S mutations in the CTD are shown by arrows. (b) The sequence of the CTH. Residues are coloured according to the scheme used in c, d and e. (c) Distribution of charged residues along the TDP-43 sequence. Negatively charged residues (Asp, D/Glu, E) are shown in red and positively charged residues (K/R) are shown in blue; there are no arginine residues present in the CTD. (d) Distribution of Gly (G) and Pro (P) residues along the sequence, indicating flexible and structure-breaking regions, respectively. (e) Distribution of Phe (F), Tyr (Y), Trp (W) and His (H) residues along the sequence. (f) Sequence-based prediction to highlight regions of TDP-43 that promote condensate formation, calculated using FuzDrop*[62–64]*, with a score above 0.6 indicating a condensate driving region. (g) Disorder propensity plot generated by protein disorder prediction system (PrDOS)*[65]*. Values above the 0.5 threshold (dashed line) indicate disordered regions, showing that the CTD residues 269-414 of the TDP-43 are predominantly intrinsically disordered. The transient α-helical region (CTH) between*

residues ~320–343 is highlighted in pink, and comprises residues with scores less than 0.5, consistent with its ability to form an ordered structure (f).

RESULTS AND DISCUSSION

Salt-Driven Expansion of the WT CTD Facilitates Condensate Assembly

Native mass spectrometric analysis of the WT TDP-43 CTD suggests that the protein populates two major conformational families, as revealed by its bimodal charge state distribution (Figure 2a). As the charge state distribution of a protein in a native IM-MS experiment reflects its solvent accessible surface area[50], we describe these two conformational families as representing more expanded conformers (charge states 18+ to 10+) and more compact states (charge states 9+ to 6+). The bimodal distribution of charge states and higher relative intensity of the more compact conformational family (~ 70 % of the measured signal) was surprising, suggesting that the TDP-43 CTD preferentially undergoes compaction, likely due to intramolecular interactions, under the conditions employed (Figure 2a). This is strikingly different to the native mass spectra of other intrinsically disordered proteins (IDPs), such as N-terminally-acetylated α-synuclein, which has a similar mass to TDP-43 CTD (α-synuclein: 14,502 Da, TDP-43 CTD: 14,889 Da) but favours more extended conformers[66]. A similar phenomenon of overly compact disordered conformations has been described previously using NMR and Förster resonance energy transfer (FRET) for eukaryotic translation initiation factor eIF4B, an intrinsically disordered protein which participates in multivalent interactions[67].

We, and others, have shown previously that ionic strength can modulate the structure and dynamics of IDPs and that these effects can be deduced by native MS[54,59,68]. Whilst the mass spectra presented here were acquired under low ionic strength conditions (20 mM ammonium acetate, pH 5.5), raising the ionic strength by addition of 150 mM NaCl[37,69] shifts the charge state distribution of the TDP-43 CTD toward higher charges (dominant 8+ to 10+; Figure 2b), indicating salt-driven chain expansion. A similar electrostatic induced expansion has been observed previously for the protein Ubiquilin-2 (UBQLN2), which forms condensates under physiological conditions[70]. Additionally, recent findings using native MS highlighted that the relative disorder content of a protein can be determined from its charge state distribution and, in the absence of ionisable residues such as lysine and arginine, the charge state distribution is dictated by the solvent accessible surface area, with the backbone amines and protein termini acting as charge carriers[71]. This is particularly relevant for low complexity domains such as the TDP-43 CTD which contains few K/R residues (Figure 1b). 20 mM ammonium acetate (pH 5.5) was selected as a standard native MS-compatible solution to preserve non-covalent interactions while minimising electrostatic screening. We have previously used 20 mM ammonium acetate for studies on α-synuclein, which is an IDP of similar molecular weight (14.5 kDa) to the TDP-43 CTD (14.6

kDa)[66,72]. Although not physiologically representative, these conditions enable interrogation of the intrinsic conformational ensemble of the CTD prior to ionic-strength modulation as a control condition. Addition of 150 mM NaCl was used to approximate physiological ionic strength, enabling assessment of electrostatic screening effects under near-cellular ionic strength conditions[73]. For these experiments we also used mildly acidic conditions, which have been shown to reduce spontaneous TDP-43 aggregation, and improve monomer stability prior to assembly assays[74].

To further investigate the structural properties of TDP-43 CTD, we used ion mobility-MS (IM-MS) to measure the collision-cross section (CCS) of each ion species. Data from travelling wave ion mobility in nitrogen gas ($^{TW}CCS_{N2}$) demonstrate that the global CCS distribution (CCSD) of TDP-43 is surprisingly monodisperse, suggesting that the TDP-43 CTD conformational landscape is tightly restricted (average $^{TW}CCS_{N2}$ of 2519 Å^2; Figure 2c). However, it should be noted that additional, more extended conformations are observed at low abundance in the CCS distribution (between 3000 and 4000 Å^2, Figure 2c). Addition of 150 mM NaCl resulted in an increase in the average $^{TW}CCS_{N2}$ of the WT TDP-43 CTD (~13% increase to 2837 Å^2), consistent with the added NaCl mediating expansion of the TDP-43 CTD chain. The CCS distributions in the presence of added NaCl are also wider (Figure 2c,d), suggesting that a more diverse array of conformers are co-populated.

It is important to note that the conformation of a protein can impact its ionisation pathway during nESI, which may influence the observed gas-phase conformations. Native/globular proteins with lower charge states have been proposed to ionise in a process described by the charged residue model (CRM), in which analytes are desolvated from shrinking droplets, and closely retain solution-like globular conformations *in vacuo*. In contrast, highly charged species are thought to arise, at least in part, from chain ejection mechanisms (CEM), whereby extended regions are expelled from droplets, potentially yielding elongated gas-phase conformations with increased surface area that may exceed their solution dimensions[75,76]. Accordingly, while we include the full charge state distribution to illustrate population redistribution across conditions, it is important to recognise that the absolute CCS values of the most highly charged states should be interpreted with some caution. Importantly, the salt-dependent conformational expansion we observe is clearly evident within the dominant low-charge (compact) ensemble (6+-10+), supporting the notion that the reported ensemble shift upon NaCl addition reflects a genuine change in solution behaviour rather than being solely a result of the nESI process.

Our data are consistent with a model whereby salt induced electrostatic screening disrupts long-range intramolecular interactions that mediate TDP-43 CTD structural collapse, to tune the conformational landscape of monomeric TDP-43 CTD. This conformational remodelling could aid in the TDP-43 CTD

forming intermolecular contacts that are critical for stabilising condensates[77] as elevated NaCl has been shown previously by others to increase the propensity of several proteins to form condensates[78–80].

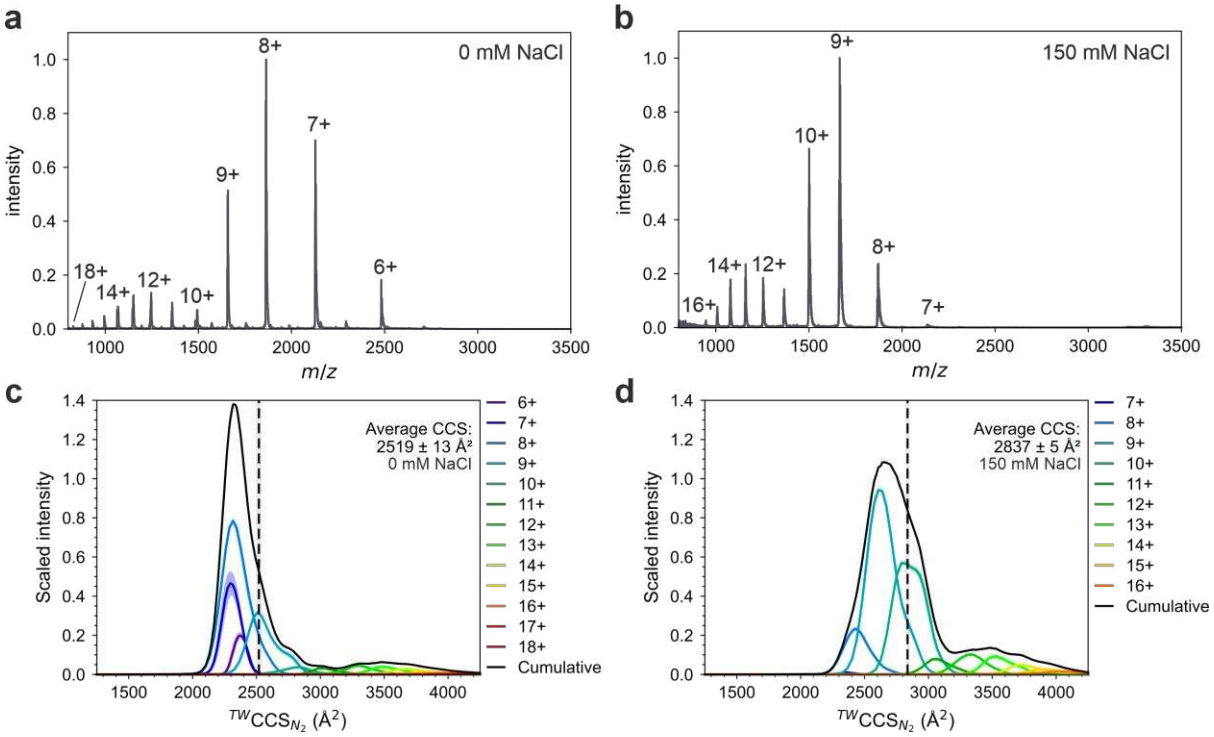

200

201 ***Figure 2. Salt-induced expansion of the TDP-43 CTD revealed by native MS, ion-mobility MS.*** *(a)*
202 *Native nanoESI mass spectrum of WT TDP-43 CTD acquired in 20 mM ammonium acetate (pH 5.5)*
203 *shows a broad charge-state distribution (6+ - 18+). (b) Native nanoESI mass spectrum of WT TDP-43*
204 *CTD acquired in 20 mM ammonium acetate (pH 5.5) with 150 mM NaCl, acquired using submicron*
205 *nanopipette nanoESI emitters*[59]*. (c) Cumulative* $^{TW}CCS_{N2}$ *distribution, showing the summed data for*
206 *each charge state in 20 mM ammonium acetate (pH 5.5), the shaded region represents the range of*
207 *three replicates. The cumulative trace (black) yields an average* $^{TW}CCS_{N2}$ *of 2519 Å² (dashed line) with*
208 *an error of ± 13 Å² giving a range of 2506-2532. (d) In 20 mM ammonium acetate (pH 5.5) with 150*
209 *mM NaCl the* $^{TW}CCS_{N2}$ *distribution shift to larger values with a broader distribution, giving an average*
210 *of 2837 Å² with an error of ± 5 Å² giving a range of 2832-2842. The grey shaded region is the standard*
211 *error from n = 3.*

The Q331K Mutation Uncouples Condensate Formation from Amyloid Assembly

Next, we set out to explore if the CTH sequence (residues 320-343) plays a role in regulating the conformational ensemble of TDP-43 CTD. We therefore designed a comparative study employing a TDP-43 CTD variant containing a known sporadic ALS-associated mutation (Q331K)[16,37,42]. As a control, we also explored the effect of another known sporadic ALS-associated mutation distal to the CTH, R361S[81].

First, we applied IM-MS to test whether the two TDP-43 CTD variants have globally similar CCSDs to the WT protein. The CCSDs of all three proteins were broadly similar, with average CCS values of WT: 2519 $Å^2$, Q331K: 2533 $Å^2$ and R361S: 2471 $Å^2$ in the absence of added NaCl (Figure 2c, 3a, 3c). Like WT TDP-43 CTD, the native mass spectra and IM-MS derived CCSDs of both variants in the presence of 150 mM NaCl suggest a conformational expansion is occurring upon addition of NaCl (~13% increase for all proteins; Figure 3a-d, Figure2c-d). A shift toward higher charge states is also observed in the native mass spectra upon addition of 150 mM NaCl (Figure S1). Combined, these data suggest that the overall conformational ensemble of WT TDP-43 CTD and the two variants studied are comparable both at low and high ionic strength.

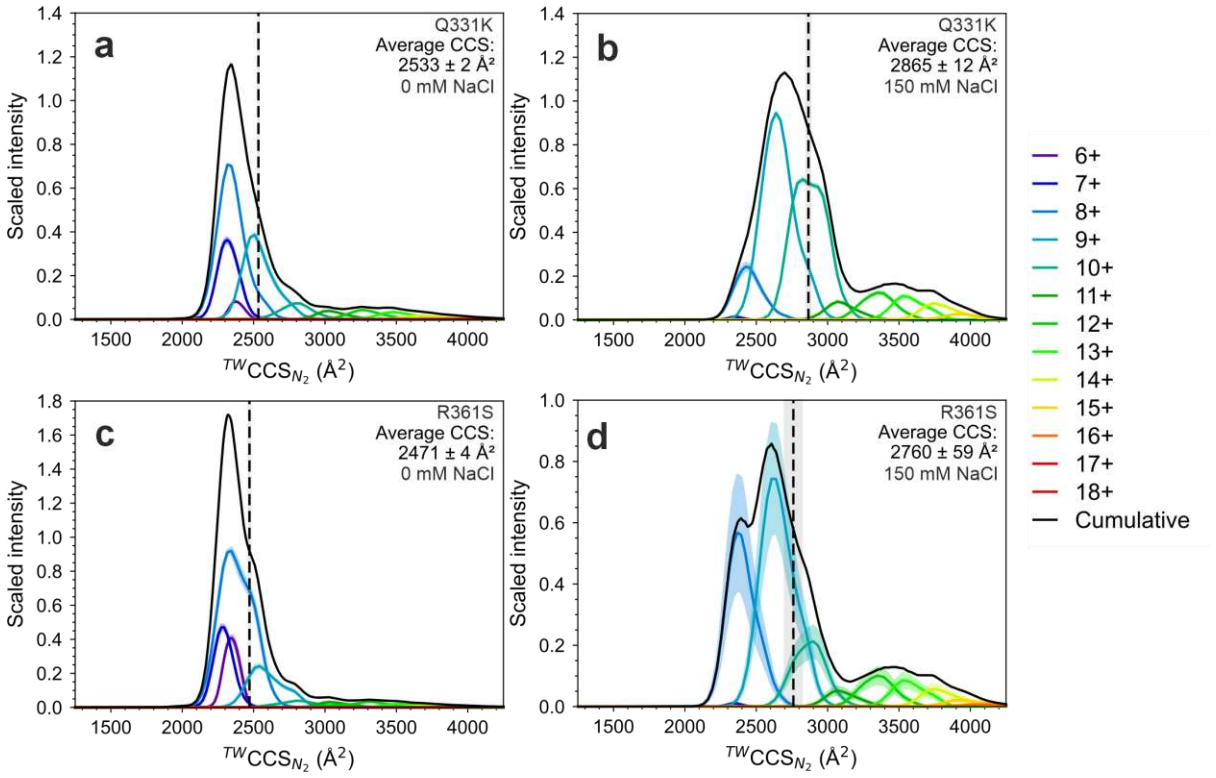

227

228 ***Figure 3 Salt induced expansion of ALS-associated variants of the TDP-43 CTD revealed using IM-MS.***

229 *$^{TW}CCS_{N2}$ ion mobility distributions for the Q331K TDP-43 CTD variant in (a) 20 mM ammonium acetate*

230 *(pH 5.5) or (b) 20 mM ammonium acetate (pH 5.5) with 150 mM NaCl. $^{TW}CCS_{N2}$ ion mobility*

231 *distributions for the R361S TDP-43 CTD variant in (c) 20 mM ammonium acetate (pH 5.5) or (d) 20 mM*

232 *ammonium acetate (pH 5.5) with 150 mM NaCl. In (a-d) the cumulative trace (black) yields an average*

233 *$^{TW}CCS_{N2}$ of the distribution plotted as a dashed black line. The grey shaded region is the standard error*

234 *from n = 3.*

Differential interference-contrast (DIC) microscopy confirmed that WT and R361S TDP-43 CTD readily formed micron-sized condensates in both the absence of NaCl and the presence of 150 mM NaCl under the solution conditions tested (Figure 4a). Q331K TDP-43 CTD did not form condensates under either solution condition tested (Figure 4a). Given this surprising observation, we next sought to further explore the condensation propensities of the Q331K variant, to determine whether condensates could be observed with increasing concentrations of protein/NaCl (Figure S2-S5). For the WT TDP-43 and R361 TDP-43 CTD variant, condensate formation was observed under all conditions tested (Figures S2, S3 and S5). In the case of the Q331K variant, condensate formation was impaired, with condensates only observed at elevated protein/NaCl concentrations (in 50 mM NaCl, a 200 μM protein concentration was required, whereas in 150 mM NaCl condensate formation was observed at protein concentrations exceeding 100 μM) (Figure S2 and S4).

These qualitative findings were quantitively confirmed using nephelometry (Figure 4b), where high levels of light scattering were observed for both WT and R361S TDP-43 CTD under both low and elevated NaCl conditions. Conversely, low levels of light scattering were measured for Q331K TDP-43 under both low and elevated NaCl conditions, consistent with the notion that this mutation abrogates condensate formation under these conditions. Intriguingly, the measured light scattering increased for both WT and R361S TDP-43 CTD when the NaCl concentration was elevated (Figure 4b) suggesting either increased propensity to form condensates and/or altered condensate size/morphology in the presence of added NaCl.

Next, we sought to determine whether the TDP-43 CTD variants retain the ability to assemble into amyloid fibrils, by performing ThT fluorescence assays under identical solution conditions to those used above. ThT interacts with the cross-β structure, characteristic of amyloid fibrils through the hydrogen bonding network of stacked β-sheets which results in immobilisation of rotational freedom of ThT molecules and subsequently fluorescence[82,83] (note that ThT is also known to interact with oligomeric species containing β-sheet content such as β-barrel structures[84,85], but here we refer to ThT kinetics being reflective of amyloid fibril assembly). Interestingly, in the absence of NaCl the Q331K variant showed a pronounced reduction in the rate of amyloid assembly compared to WT and R361S TDP-43 CTD (Figure 4c,d) with an increase in ThT fluorescence observed after around 40 hours, consistent with delayed aggregation by this variant. Note that there is some degree of variation of kinetics observed for R361S TDP-43 CTD (Figure 4c) which we have not explored further, and we postulate may be due to heterogeneity in the degree of condensate assembly in different sample wells. The addition of 150 mM NaCl rescued the ability of Q331K TDP-43 CTD to form amyloid fibrils (Figure 4c,d), despite the protein not forming condensates under these conditions. Interestingly, the WT TDP-43 CTD appeared to exhibit slower amyloid assembly kinetics upon addition of NaCl, a

phenomenon also observed recently for the protein A1-LCD which is the prion-like LCD of heterogeneous nuclear ribonucleoprotein A1 (hnRNPA1)[86].

To assess the effect of ionic strength compared with NaCl addition specifically, we measured condensate propensity and amyloid assembly in 170 mM ammonium acetate to match the addition of 150 mM NaCl to 20 mM ammonium acetate (total ionic strength in both cases of 170 mM). We found that the Q331K variant again did not assemble into condensates (Figure S6 and S7), but that amyloid formation still occurred under these elevated ionic strength conditions (Figure S8), akin to the situation observed where amyloid formation could be tuned by addition of NaCl (Figure 4c,d). This suggests that it is unlikely that the effects observed are due to Na^+ and Cl^- ion binding specifically. We also observed that the WT TDP-43 CTD formed amyloid much faster in 170 mM ammonium acetate than under identical ion strength conditions but in the presence of NaCl (compare Figure 4d and Figure S8) which suggests that different ions may alter amyloid assembly differently. Additionally, we explored the role of condensate assembly by the WT TDP-43 CTD on the rate of amyloid assembly by adding 5 % v/v 1,6-hexanediol, which is known to dissolve biomolecular condensates[87]. It has been observed that in the case of protein A1-LCD biomolecular condensates act as metastable sinks that divert proteins away from forming amyloid because condensate interiors suppress nucleation and fibril growth[86]. Here, we observe a similar effect for TDP-43 CTD, as when condensate assembly is suppressed by the addition of 5 % (v/v) 1,6-hexanediol the rate of amyloid assembly of the WT TDP-43 CTD is dramatically increased (Figure S9).

Combined, these data suggest that two independent amyloid assembly routes exist for the TDP-43 CTD variants: a condensate-mediated pathway, and a salt-driven pathway that does not require condensate formation, but both involve conformational expansion of the monomeric precursor to initiate each assembly process.

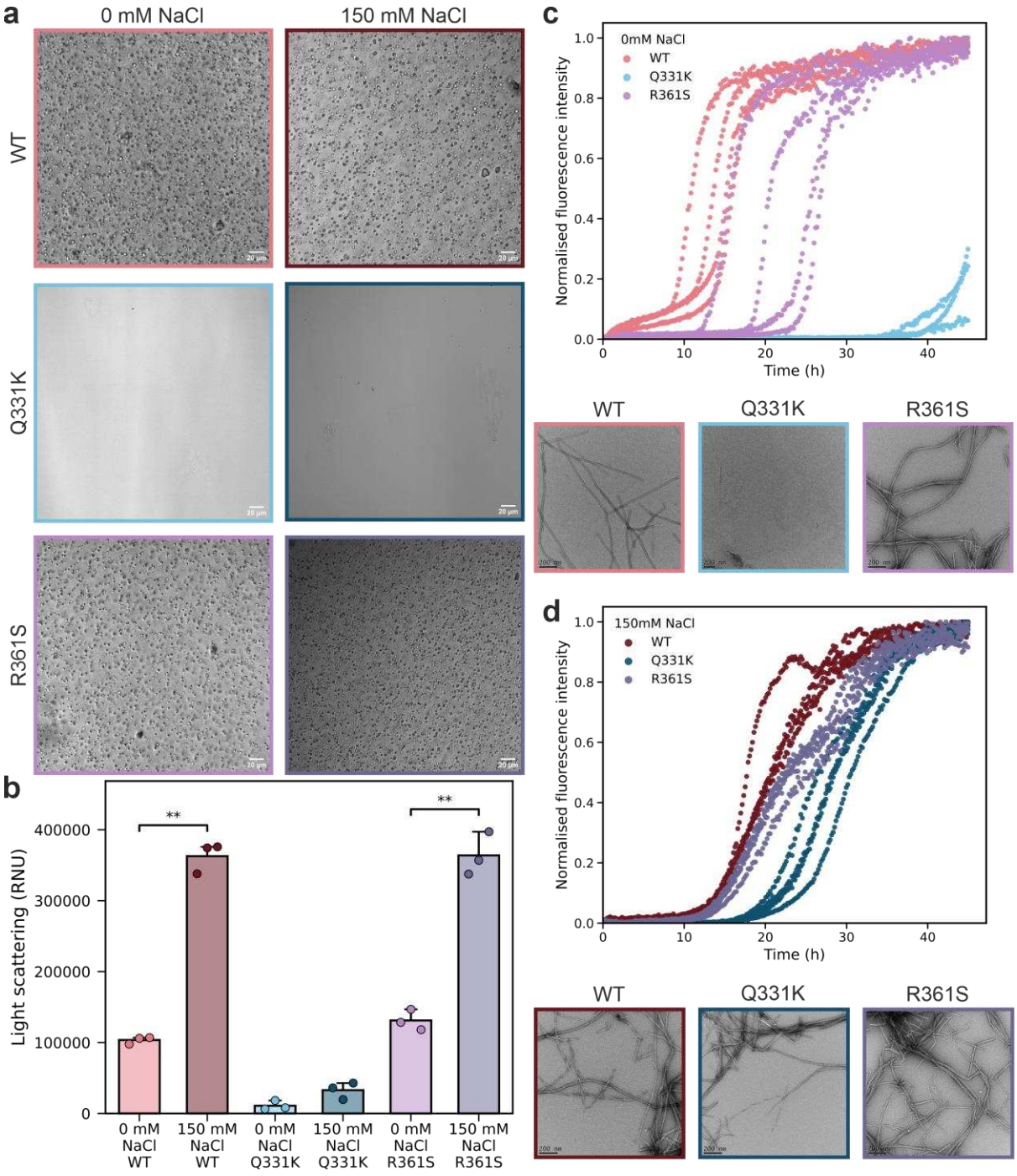

Figure 4. Point mutations and ionic strength differentially tune TDP-43 CTD condensate formation and amyloid assembly. *(a) Differential-interference-contrast images of the WT TDP-43 CTD in 0 mM NaCl (light red) and 150 mM NaCl (dark red), the Q331K TDP-43 CTD in 0 mM NaCl (light blue) and 150 mM NaCl (dark blue), the R361S TDP-43 CTD in 0 mM NaCl (light purple) and 150 mM NaCl (dark purple). Scale bars = 20 µm. Protein concentration was 50 µM measured in 20 mM ammonium acetate, pH 5.5. (b) Nephelometry light scattering measurements (n = 3) after 10-hour incubation. An unpaired two-sided Welch's T-test was performed for significance where ** = p < 0.01 (c,d) ThT fluorescence kinetics of amyloid formation at 0 mM (c) and 150 mM (d) NaCl (n = 4) (upper panels). The insets (lower*

panels) are representative TEM images which were taken at the timepoint where WT reached maximal fluorescence (scale bar = 200 nm) showing amyloid fibrils recovered at the end points of the assembly reactions.

Next, we subjected the 7+ charge state of the three CTD variants from native mass spectrometry to collision-induced unfolding (CIU; Figure 5) to investigate whether differences in gas phase stabilities between variants could be observed. We chose this charge state because it was an abundant lowly-charged species that was present in all the mass spectra we acquired, and therefore these data will reflect unfolding from the most compact state. CIU experiments were performed under low ionic strength conditions (20 mM ammonium acetate) to ensure that the protein remained monomeric and to maintain a stable electrospray. Attempts to perform CIU under elevated ionic strength (150 mM NaCl or 170 mM ammonium acetate) were hindered by rapid phase separation and aggregation over the extended acquisition period required for sequential voltage ramps, preventing reproducible measurement. CIU was therefore only used here to assess intrinsic conformational stability differences between variants in the absence of salt. Previous work has demonstrated that, for folded proteins, the number of unfolding transitions in a CIU experiment is correlated with the number of folded domains, and that the voltage required to elicit unfolding can (relatively) correlate with domain stability[88,89]. The WT CTD was observed to undergo an unfolding transition at ~ 55 V. Interestingly, the Q331K variant underwent an unfolding transition at markedly lower energy (~ 30 V). In contrast, the R361S mutant exhibited a much higher stability with evidence of an initial transition occurring at ~ 60 V. These fingerprints, acquired in the absence of salt, establish a stability order of R361S > WT > Q331K, reflecting the order of *in vitro* condensation propensity observed by nephelometry (Figure 4f). Transition midpoints (CIU50 values) were determining by fixing drift time windows corresponding to native and activated species. For WT and R361S TDP-43 CTD a full transition to activated species was not observed, and therefore we quantitatively measured CIU50*, which corresponds to 50% of the observed transition (~50 V; Figure 5a,c). To observe a complete transition, an collision voltage greater than 60 V was required however this resulted in fragmentation of the proteins and loss of signal. A complete transition for Q331K was observed with a CIU50 of ~ 40 V (Figure 5b). We interpret these data as evidence that the Q331K substitution perturbs the structural stability of CTH as a result of the mutation to a positive charge. Rather than implying a simple relationship between increased disorder and reduced aggregation, we propose that the CTH may function as a structured interaction element that contributes to productive intermolecular contacts during condensate formation. Destabilisation of this region by the Q331K mutation may therefore reduce helix-mediated interactions required for condensate assembly. Additionally, the introduction of a lysine at position 331 alters local charge patterning, which may independently influence intermolecular association and solubility.

These data demonstrate that CIU can provide a rapid mass-spectrometric read-out of how single-site mutations remodel the conformational landscape of an intrinsically disordered, amyloid-prone region, even when a global CCS analysis (Figure 2,3) does not suggest any gross structural changes are occurring.

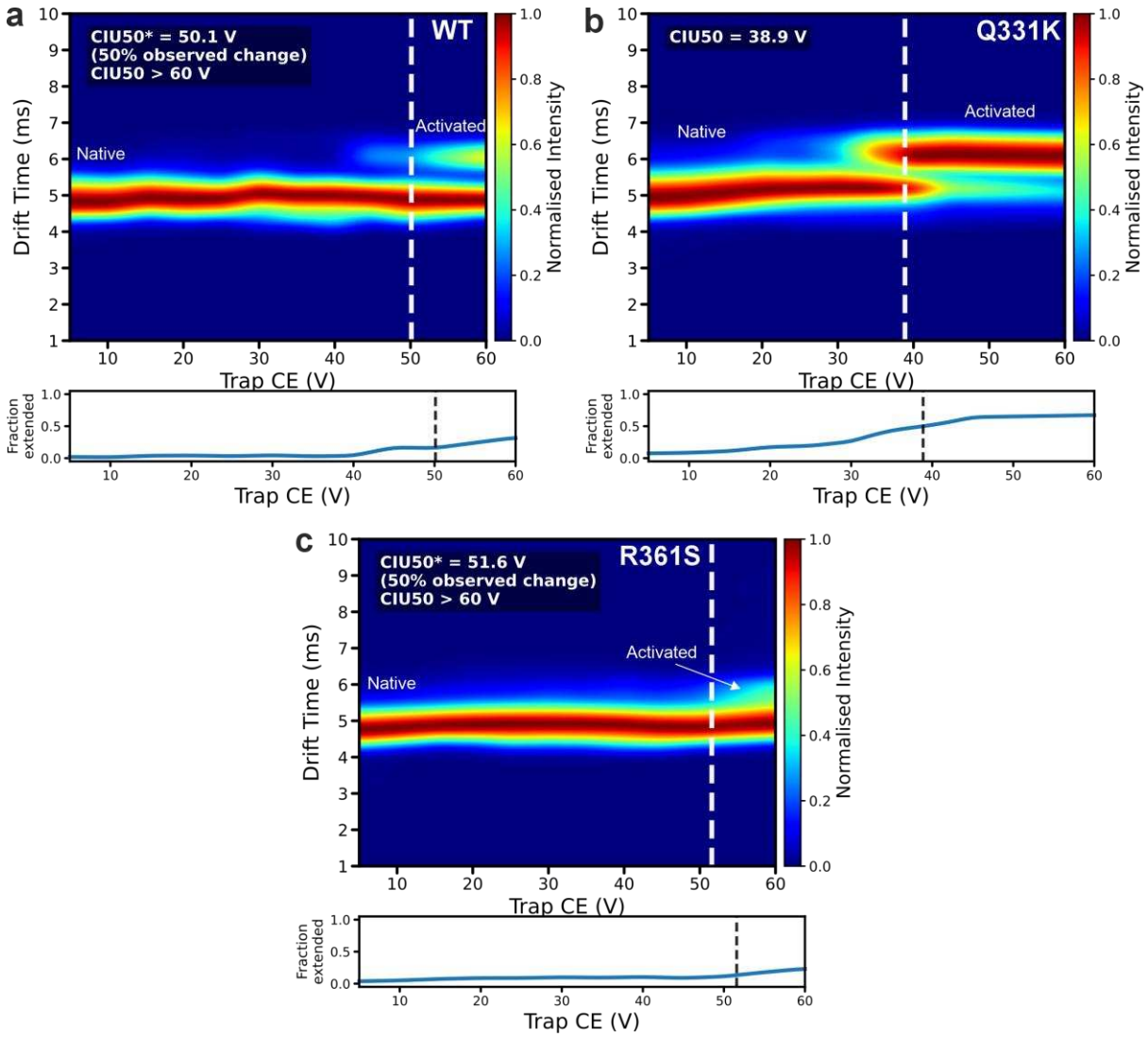

Figure 5. Collision-induced unfolding (CIU) fingerprints highlight helix-dependent stability of TDP-43 CTD variants. *Normalized heat-maps show drift time (ms; y-axis) as a function of trap collision energy (CE in V, x-axis) for the 7+ charge state of the WT, Q331K, and R361S TDP-43 CTD (see Methods). Colour scale (right; z-axis) denotes signal intensity. Dotted lines are shown to guide the eye and indicate the two conformations. The native conformation was restricted to a drift time window of ~ 4.0 – 5.5 ms and the activated conformation 5.6 – 7.0 ms for CIU50 and CIU50* calculation. CIU50* represents 50% of the observed change as determined by normalised intensities, plotted as fraction extended below each heat map.*

Coarse-grained molecular dynamics simulations capture the altered condensation properties of Q331K TDP-43 CTD

Following from our *in vitro* observations we applied coarse-grained molecular dynamics using the CALVADOS2 force field, which applies a one-bead-per-residue model to describe the behaviour of multi-chain conformational ensembles of IDPs, to perform slab simulations of the TDP-43 CTD and model its phase separation behaviour[90]. To ensure consistency with experimental conditions, CALVADOS2 slab simulations were performed at pH 5.5 and at low ionic strength (20 mM) and high ionic strength (170 mM), matching the IM-MS and in vitro assays. We note that CALVADOS2 treats the CTD as intrinsically disordered and does not explicitly model the CTH or potential helix-helix packing interactions. Therefore, simulation-derived conclusions regarding overall condensate propensity and interaction balance within the dense phase are considered robust, whereas specific residue-residue contact patterns involving the CTH region should be regarded as hypothesis-generating. Given that the CTH is transient in solution[16] and its structural state within condensates remains unresolved, the simulations are interpreted as probing condensate stability and intermolecular interaction balance after phase separation rather than helix-driven nucleation events. Nevertheless, in these simulations, the WT and R361S TDP-43 CTD variants readily formed condensates, producing a single dense phase and a dilute phase (Figure 6a,b). By contrast, the Q331K variant formed condensates to a lesser extent (Figure 6a,b), consistent with our DIC and nephelometry measurements (Figure 4a,b). The one-dimensional density profiles (Figure 6b) quantify this observation, wherein, at low ionic strength the WT and R361S TDP-43 variants display clear dense- and dilute-phase plateaus, whereas the profile for the Q331K variant remains near dilute-phase levels throughout the simulation window. Elevating the ionic strength increases the dense-phase concentration and reduces the dilute-phase concentration for all variants (Figure 6b).

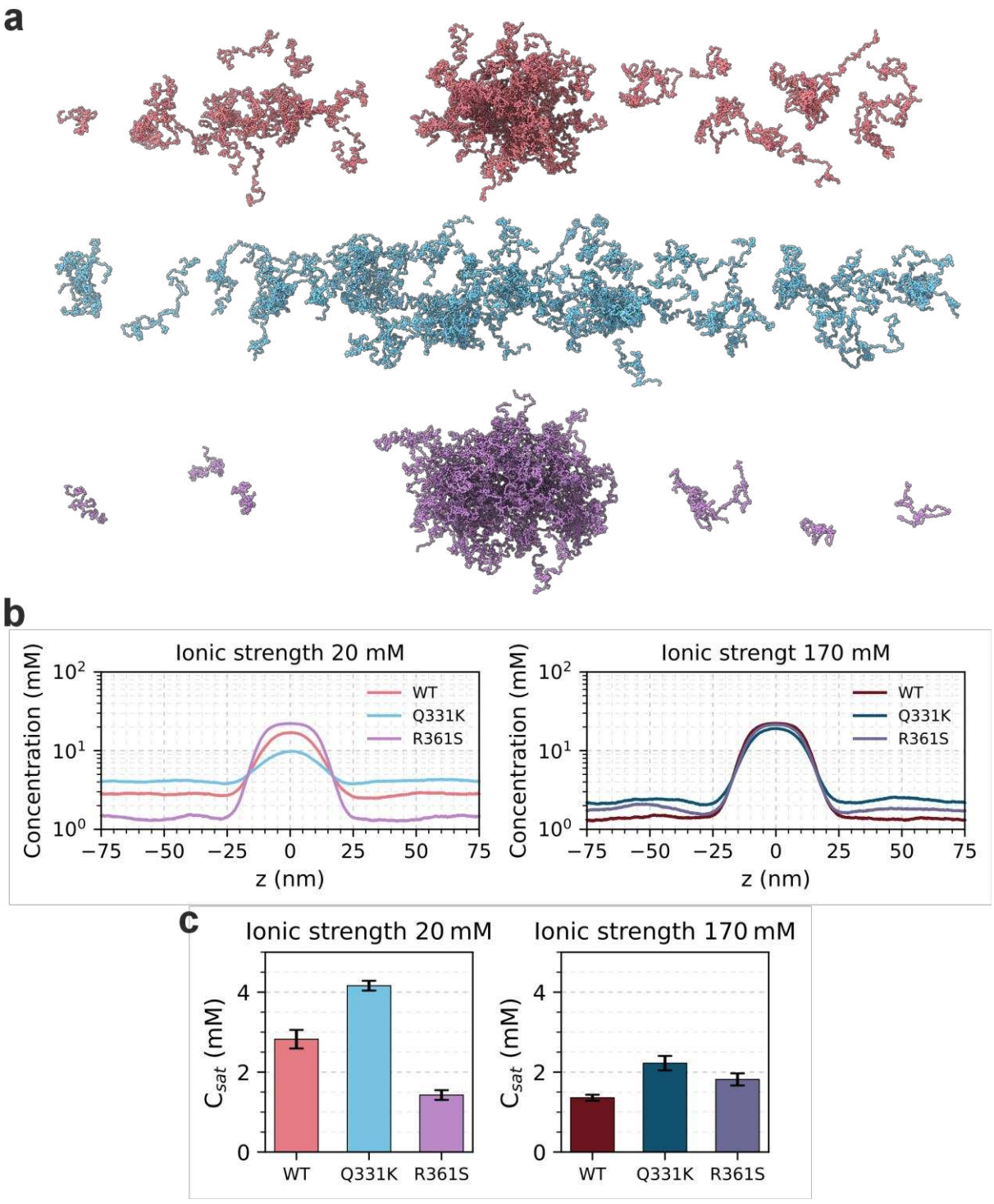

Figure 6. CALVADOS simulations capture salt-tuned phase for the TDP-43 CTD. *(a) Representative slab snapshots from CALVADOS simulations for WT (top), Q331K (middle) and R361S (bottom) TDP-43 CTD. (b) The average concentration of protein across the z-axis of the slab simulation, for simulations performed at low (upper panel) and high (lower panel) ionic strength. (c) Calculation of C_{sat} from the region of the simulation outside of the dense phase in the z-axis.*

From these data we can extract a saturation concentration required to yield a condensate core (C_{sat}; Figure 6c). These C_{sat} values mimic the hierarchy of condensate propensity we observed experimentally (R361S > WT > Q331K; Figure 4). We also plotted homotypic contacts maps for the WT TDP-43 CTD at 20 mM and 170 mM ionic strength, respectively (Figure 7a,b), which are generated by taking the TDP-43 CTD molecule which is closest to the centre of the dense phase in the z-axis of the CALVADOS slab simulation and therefore represents a molecule at the centre of the condensate. We then calculated its residue contacts to all other CTD molecules around it. We performed our analysis in this way to exclude any molecules at the edges of the slab. We observe that N- and C-termini interact between molecules under low ionic strength conditions (20 mM; N and C terminal residues have highest contact intensities in Figure 7a) and that intermolecular interactions increase under elevated ionic strength conditions (170 mM), as reflected by higher contact intensities throughout the sequence (Figure 7b). This is consistent with elevated NaCl levels promoting condensate formation. Similar findings were observed for the Q331K and the R361S variants (Figure S10).

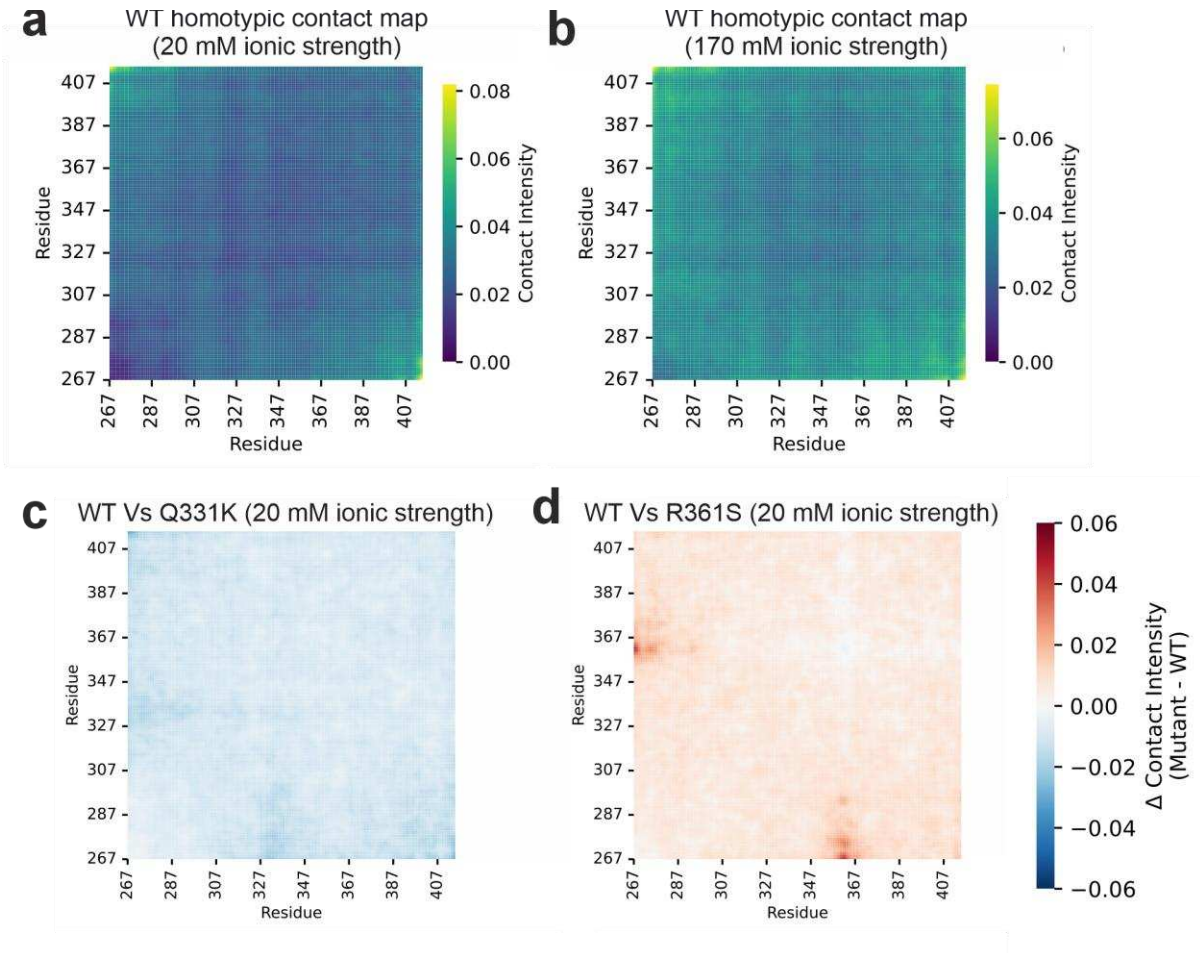

Figure 7. CALVADOS simulations map salt-tuned contact networks in the TDP-43 CTD and changes in homotypic interactions in TDP-43 CTD variants. *(a,b) Homotypic residue-residue contact maps for WT TDP-43 CTD at (a) 20 mM and (b) 170 mM ionic strength. (c,d) Differential homotypic residue-*

residue contacts maps in 20 mM ionic strength conditions when comparing (a) Q331K with WT TDP-43 CTD and (b) R361S TDP-43 with WT TDP-43 CTD.

Difference contact maps were plotted to compare the contact maps for WT TDP-43 CTD with those for the Q331K at 20 mM and 170 mM ionic strength conditions, respectively (Figure 7c, Figure S11) and R361S (Figure 7d, Figure S11) variants. These demonstrate that intermolecular interactions are reduced for the Q331K mutant compared to WT TDP-43 CTD, with the biggest differences in interactions with the N-terminus being in residues that include the mutation site (Q327-M414; Figure S12). We propose that this is because interactions with the positively charged N-terminus of the chain are reduced because of the introduced Lys residue. These data are consistent with our observation that the Q331K variant of TDP-43 CTD has reduced propensity to form condensates *in vitro* (Figure 4). Conversely, intermolecular contacts are increased across the sequence for the R361S variant compared to WT TDP-43 under low ionic strength (20 mM; Figure 8c), with the biggest differences occurring in residues M359-A366 (Figure S12). This region includes the Ser residue that has been added, and we propose that this substitution promotes interactions with the positive N-terminus. Whereas, at high ionic strength (170 mM; Figure S11) the differences are reduced suggesting that WT and R361S TDP-43 CTD behave more similarly under this condition.

In summary, these coarse-grained molecular dynamics slab simulations using the CALVADOS2 forcefield recapitulated *in vitro* measurements of condensate propensity (Figure 3) demonstrating a hierarchy for condensate propensity of: Q331K < WT < R361S. This observation is consistent with recent benchmarking that demonstrates the model's ability to order relative propensities of IDPs to form biomolecular condensates[91]. However, CALVADOS omits the known α-helical structure of the CTH and therefore could be underestimating the solubilising effect of the helix for WT/R361S, while overestimating the condensate propensity of Q331K, which introduces an extra positive charge and might prevent dimerization via helix-helix interactions[16].

DISCUSSION

It has been reported previously that the CTH within the TDP-43 CTD is integral for facilitating inter-protein interactions which stabilise biomolecular condensates[16,37]. Here, we have explored how a single mutation (Q331K) in the CTH controls the TDP-43 CTD conformational ensemble, its amyloid fibril formation kinetics and propensity to form biomolecular condensates using an integrative approach. Studying this variant has enabled us to demonstrate that it is possible to uncouple amyloid assembly from biomolecular condensate formation by a single residue substitution in the CTH associated with disease, suggesting that the TDP-43 CTD can form amyloid fibrils by two mutually-exclusive routes (Figure 8).

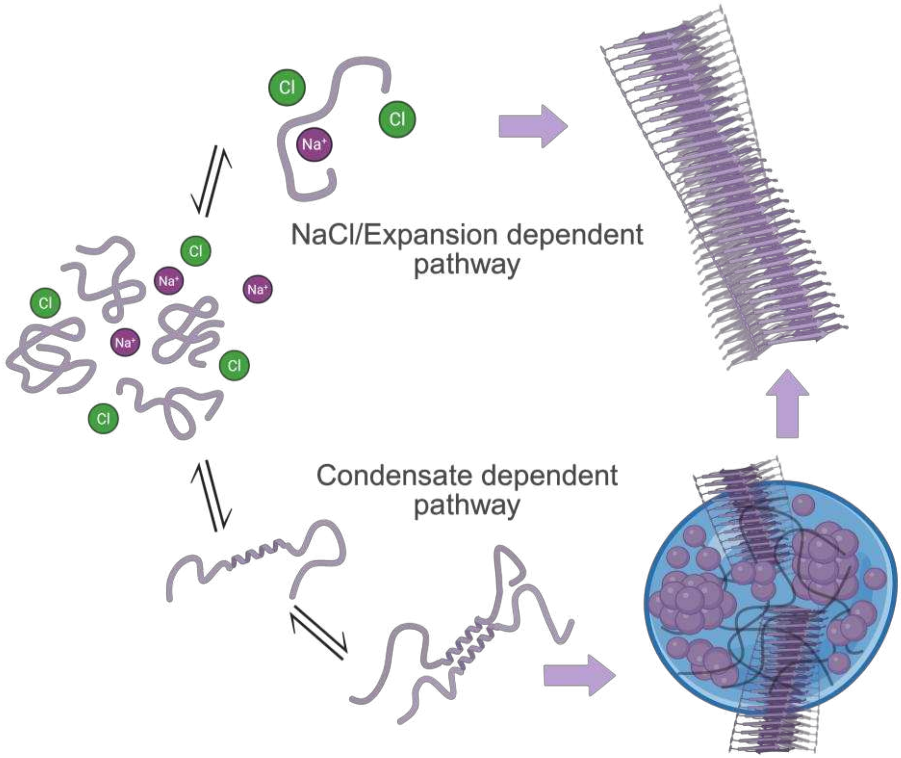

Figure 8. Model of dual amyloid assembly pathways of TDP-43 CTD. *A schematic depicting two possible routes to amyloid assembly. In the upper pathway, amyloid formation proceeds from solution and is accelerated by the addition of NaCl which increases the abundance of expanded TDP-43 CTD conformations. In the lower pathway, CTH-mediated interactions stabilise TDP-43 CTD condensates and this precedes amyloid assembly. Arrows indicate the direction of structural progression.*

In this study we employed submicron nanopipette nanoESI emitters which uniquely enable native MS studies in high ionic strength buffers. This builds on our recent work studying the protein α-synuclein[59], and the work of others who have shown the many benefits of using sub-micron emitters for native MS [57,58,92,93]. Here, our native IM-MS data show that addition of NaCl increases the population of more

extended conformations of the TDP-43 CTD monomer (Figure 2a-d), suggesting that salt perturbs intramolecular interactions. This is consistent with the general principle that electrostatic screening weakens long-range intramolecular interactions, resulting in expansion of IDP structures/ensembles, therefore priming the protein chain to instead form intermolecular interactions[86,94]. Although the CTH helix is not explicitly modelled in our coarse-grained simulations (Figure 6, Figure 7 and Figure 8), the results nevertheless recapitulate our *in vitro* data. While helix formation has been shown to play a role in promoting phase separation[16], our findings suggest that the helical structure may not need to be present *in silico* to model how mutations alter TDP-43 CTD condensation propensity.

Strikingly, the Q331K mutation within the CTH abolished condensate formation under both solution conditions used in our amyloid assembly kinetics analyses, whereas the mutation R361S, which lies outside of the CTH did not (Figure 4). Despite condensate assembly being perturbed by this single point mutation, we show that Q331K TDP-43 CTD amyloid fibrils still form from bulk solution in the absence of pre-formed condensates, and that amyloid formation by this route/variant can be accelerated by addition of NaCl (Figure 4c-d). Our native IM-MS data demonstrate that in the absence of NaCl, monomeric TDP-43 CTD populates relatively compact conformations, and that added NaCl promotes chain expansion (Figure 3), possibly via electrostatic screening[95–97]. This suggests that conformational expansion is required to initiate TDP-43 CTD fibrillation from the monomeric protein in bulk solution. This is consistent with data from single-molecule FRET and simulations that together have shown that intrinsically disordered proteins adopt more expanded conformations in the dense phase of condensates (in a system comprising histone H1 and ProTα) [98]. We hypothesise that the conformational expansion of TDP-43 CTD observed in condensates is akin to the conformational expansion occurring in bulk for the Q331K variant upon NaCl addition, and both act to facilitate amyloid assembly via different mechanisms/material states.

Despite our observation of chain extension under elevated salt conditions in our IM-MS experiments (Figure 2c-d), the WT CTD formed amyloid more slowly than at lower ionic strength, as measured by the length of the lag phase (Figure 4d). We interpret this observation as evidence of the competition between pathways where this promotes partitioning of monomers into condensates thereby depleting amyloid-competent species from the bulk. Interestingly, when 1,6-hexandediol, known to dissolve condensates by weakening hydrophobic interactions, was added at 5% (v/v) under high salt concentrations, ThT positive amyloid assembly was accelerated for the WT CTD (Figure S9). Under these conditions, the effective bulk concentration of amyloid-competent precursors presumably is increased, removing the kinetic "sink" imposed by condensates[86]. Together, these data support a model involving competing mechanisms towards amyloid assembly in which for the WT and R361S TDP-43 CTD variants, elevated salt favours a condensate-dominant route that is kinetically slower in

amyloid formation, whereas dissolution of condensates redirects the system to the salt-expanded, fibril forming pathway (Figure 8)[86]. This model is consistent with the data we have obtained for the Q331K TDP-43 CTD variant, as in the absence of added NaCl amyloid assembly is dramatically retarded, and our IM-MS is consistent with compact conformations predominating. However, increasing the NaCl levels accelerates amyloid assembly and promotes a conformational expansion of the protein, without triggering condensate formation.

Transient secondary structural elements are known to act as "stickers" that participate in intermolecular interactions to form condensates. In TDP-43, residues ~320–343 form the metastable CTH that mediates helix-helix contacts and contacts with glycine/serine-rich regions[15,38,43]. Multiple studies have shown that enhancing helical propensity in this region increases the propensity for condensate formation, whereas helix-breaking substitutions reduce it[16,37]. Residue Q331 lies within the CTH. The Lys substitution at residue 331 (Q331K) perturbs both charge patterning and helical stability: it introduces a local positive charge, alters the helix macrodipole/side-chain packing, and disrupts helix-helix pairing[16,37,43]. Our findings align with prior reports that mutations within CTH tune condensate formation, highlighting the CTH as a molecular switch that gates access to facilitate condensate assembly[37]. Here we extend this further by revealing how such alterations also tune amyloidogenicity.

Much is known about the complex interplay between amyloid assembly and condensate formation. Condensate assembly can increase local concentration in the dense phase by 10-1000x[99,100], yet the dense phase is known to sequester monomers, slowing fibril assembly dependent on protein sequence, salt, pH and RNA presence[86,101]. Given that our IM-MS measurements of WT and R361S TDP-43 were taken under conditions where condensates were present, it is not possible for us to determine if the protein signal detected corresponds to monomer present in the bulk phase surrounding the condensates, or protein ejected from the condensates during ionisation.

Whilst our IM-MS derived CCSD analysis of the three TDP-43 variants revealed they adopted broadly similar structural ensembles (Figure 2, 3), CIU measurements did reveal stability differences (Figure 5). Given the correlation of the number of CIU unfolding events with structured domains in proteins, the CIU fingerprints (Figure 5) could represent unfolding of the CTH but also unfolding via disruption of long-range intramolecular interactions which stabilise the over-compact protein conformation of TDP-43 CTD (Figures 2 and 3). Interestingly, the Q331K variant presented a much less stable CIU fingerprint (for the 7+ charge state) than the WT protein (Figure 5) which might reflect weaker intramolecular interactions formed when a positive charge is added at this site in the CTH, which is also reflected in our protein-protein interaction maps (Figure 6e,f). This demonstrates that by

combining global CCSD analysis with CIU experiments, it is possible to unpick subtle conformational changes in disordered proteins using native MS.

It is important to note that the situation in vivo/in cell is much more complex than our in vitro experiments, with co-condensation known to play pivotal roles in cellular condensate assembly[102]. Molecular chaperones such as HSP70 and HSP40[103,104] and other client biomolecules such as RNA can partition into condensates where they can bind to sticker motifs on proteins undergoing condensate assembly to increase fluidity of the dense phase. Hsp70 has been shown to partition into condensates and chaperone condensed Fused in sarcoma (FUS) protein to prevent amyloid conversion, and when Hsp70 is depleted, condensates undergo a liquid-to-solid transition, and amyloid assembly ensues[103]. Additionally, in a cellular context, as well as the assembly of multicomponent condensates, PTMs, crowding and ionic composition may also play a role in deciding amyloid assembly pathways. Combined, these factors add to the complexity that must be explored if we are to fully understand the mechanisms that govern condensate mediated amyloid assembly. While bulk cytosolic ionic strength and pH are tightly regulated under homeostasis, cellular stress (oxidative stress, osmotic challenge, or stress granule formation) can locally alter ion strength, protonation states, and electrostatic screening. These changes can modulate the balance between intramolecular contacts and intermolecular interactions, thereby shifting TDP-43 from a condensate-mediated assembly route toward a salt-expanded amyloid pathway under conditions that mimic the altered physicochemical environments associated with stress responses.

Although our data support electrostatic screening as a mechanism by which ionic strength modulates CTD expansion and condensate assembly, we have not systematically explored ion-specific effects including Hofmeister ordering and multivalent cations. Future work systematically varying ion identity and valency will therefore be essential to distinguish purely electrostatic screening effects from ion-specific modulation of TDP-43 condensate assembly and fibrillation.

CONCLUSION

Our integrative analysis combining native mass spectrometry, biochemical characterisation supported by coarse-grained MD simulations identifies the sequence of the CTH of TDP-43 as the decisive element that couples condensate formation with amyloid assembly. This mechanistic framework reveals competing self-assembly pathways towards amyloid assembly and suggests that understanding the molecular mechanisms that govern the choice between alternative self-assembly pathways might be crucial for elucidating disease mechanisms.

METHODS

Recombinant TDP-43 CTD expression and purification

A plasmid containing the DNA sequence for the C-terminal domain of TDP-43 (residues 267- 414) was kindly gifted from Nicolas Fawzi (Addgene plasmid #98669) and mutations Q331K and R361S were introduced by site-directed mutagenesis (Q5® site-directed mutagenesis kit, New England Biolabs). For protein expression, chemically competent BL21 DE3 *E. coli* cells were transformed with plasmids containing the TDP-43 CTD gene. Cells were grown in LB media with kanamycin (50 µg/mL) at 37 ˚C with shaking (200 rpm) to an OD_{600} of 0.6, and protein expression was induced by the addition of 0.01 mg/mL Isopropyl β-D-1-thiogalactopyranoside (IPTG) for 4 hr at 37°C, 200 rpm. Cells were harvested by centrifugation, resuspended in lysis buffer (20 mM Tris-Cl, 300 mM NaCl, 10 mM Imidazole, 1 mM DTT, pH 8.0) supplemented with EDTA-free protease inhibitor cocktail (Roche) and lysed using a cell disruptor (Constant cell disruption systems). The lysate was centrifuged (20,000 xg, 60 min) and the insoluble material, including inclusion bodies (IBs) containing the expressed TDP-43 CTD, was resuspended in denaturing binding buffer (20 mM Tris-Cl, 300 mM NaCl, 10 mM Imidazole, 1 mM DTT, 8 M Urea, pH 8.0). The solubilised IBs were centrifuged (20,000 xg, 60 min) to remove remaining insoluble debris and then applied to a 5 mL Histrap HP column (Cytiva). The column was washed with 5 column volumes of binding buffer, before elution with a linear gradient (0-100% B) of buffer B (20 mM Tris-Cl, 300 mM NaCl, 500 mM Imidazole, 1 mM DTT, 8M Urea, pH 8.0) over 20 column volumes. For His-tag cleavage, the protein was incubated with Tobacco Etch Virus (TEV) (1:25 w/w) protease at 4°C overnight whilst dialysing into 20 mM MES buffer, pH 5.5. Cleaved protein was resuspended in denaturing binding buffer and reapplied to a 5 mL Histrap HP column (Cytiva). The flow through was collected and concentrated to ~ 1 mM using Amicon® 10 kDa ultra centrifugal filter units (Merck Millipore, Darmstadt, Germany) before being snap-frozen and stored at – 80 °C. Aliquots were stored at high protein concentrations (~1 mM) in 8 M urea to prevent aggregation and condensate assembly, and were diluted into 20 mM ammonium acetate, pH 5.5 immediately prior to analyses. Analyses were carried out at pH 5.5 to maintain protein solubility, consistent with previous studies[74,105].

Nanopipette nanoESI Emitter fabrication

The nanopipette nanoESI emitter tips were fabricated using 1.0 mm outer diameter and 0.5 mm inner diameter quartz capillaries (QF100-50-7.5; Sutter Instrument) using the Sutter Instrument P2000 laser puller (World Precision Instruments). A two-line protocol was used: line 1 with HEAT 750/FIL 4/VEL 30/DEL 150/PUL 80, followed by line 2 with HEAT 850/FIL 3/VEL 40/DEL 135/PUL 225. This protocol generates nanopipettes with openings of ~40nm in diameter[59]. The pulling protocol is specific to the instrument and can vary between different pullers, so individual optimisation of the protocol is needed in each laboratory. For native MS emitters were filled with analyte solution and fitted with a platinum wire (PT00-WR-000117; Goodfellow) prior to use.

Native ion mobility mass spectrometry

Native IM-MS experiments were performed on a Synapt G2-Si HDMS mass spectrometer (Waters Corporation, Wilmslow, UK) with travelling (T-wave) ion mobility and a nano-ESI source. TDP-43 CTD variants (WT, Q331K, R361S) were analysed at a concentration of 10 µM in 20 mM ammonium acetate[59,66,72], pH 5.5. Instrument parameters were as follows: capillary voltage 1-1.4 kV, source temperature 30 °C, sampling cone 18 V, trap collision energy 5 V, transfer collision energy 2.0 V, trap DC bias 30 V, IM wave velocity 550 m/s, IM wave height 10 V. The trap gas flow was 2.0 mL/min, IMS gas flow was 6.0 mL/min (using N_2 gas) and the helium gas flow was 80.0 mL/min. The IM spectra were calibrated[106] using denatured cytochrome c (charge states 13+ to 19+), myoglobin (charge states 15+ to 24+) and ubiquitin (charge states 7+ to 13+), 10 µM solutions of each calibrant in 50 % (v/v) acetonitrile, 0.1 % (v/v) formic acid were used for calibration) to obtain CCS distributions for each TDP-43 CTD charge state detected. Here we term these values $^{TW}CCS_{N2}$, consistent with community standards[106], signifying that the CCS values were calculated using traveling wave ion mobility in N_2 buffer gas using calibrants acquired in N_2 buffer gas. Note that for calibration of our travelling wave IM data, we have used denatured protein standards. Our rationale for this choice is that TDP-43 is an intrinsically disordered protein and therefore unfolded/denatured proteins could be more reflective of the structural properties of the protein compared with natively folded proteins[107–110]. It is important to note that calibrant choice can influence the calibrated CCS values obtained from travelling wave IM experiments, and we have carefully chosen appropriate calibrants that span the *m/z* and drift time values of the analytes investigated in this work[106,111]. MassLynx v4.1 (Waters Corporation) was used for data processing. For collision induced unfolding (CIU), instrument parameters were identical except for the trap collision energy which was systematically increased from 5 V to 60 V in 5 V increments. Arrival time distributions for the 7+ charge state were selected to generate CIU plots. Drift time profiles were extracted at each collision voltage from the spectral peak using the full width of the peak at half maximum (FWHM) intensity.

ThT amyloid assembly kinetics

Kinetics of TDP-43 CTD amyloid formation were monitored in a 96-well, non-binding, flat-bottom microplate (Corning; 10438082). Samples (100 µL) containing 50 µM protein with 20 µM Thioflavin T (ThT) in 20 mM ammonium acetate, pH 5.5 with 0 mM NaCl and 150 mM NaCl were incubated at room temperature, quiescently in a FLUOstar Omega plate reader (BMG Labtech). Fluorescence intensity was measured by exciting at 440 ± 10 nm and collecting emission at 482 ± 12 nm using a bandpass filter. Four replicate measurements were conducted, and results were blank corrected and normalised to the maximum fluorescence value of each curve except for when amyloid formation did not occur

(in the case of Q331K TDP-43 CTD variant in the absence of added NaCl) where the curve was normalised to the maximum intensity measured for WT TDP-43 CTD in the absence of salt.

Negative Stain Transmission Electron Microscopy

A sample of 5 µL was taken from the ThT plate at the endpoint of each reaction, loaded onto a glow discharged (30s, Pelco Easi-glow), 400 mesh continuous carbon grid, and incubated for 2 min. The sample was blotted and washed twice with H_2O before being blotted and stained twice with 2% (w/v) uranyl acetate. Grids were imaged on FEI Tecnai T12 electron microscope using a nominal magnification of 30,000×.

DIC microscopy

100 µL of the TDP-43 CTD (WT, Q331K or R361S) protein was added at a concentration of 50 µM, in 20 mM ammonium acetate, pH 5.5 containing 0 mM or 150 mM NaCl to individual wells of an 18-well high glass bottom chamber slide (Ibidi). To generate phase diagrams, 10 µM, 50 µM, 100µM and 200 µM was imaged at 0 mM, 50 mM and 150 mM NaCl in 20 mM ammonium acetate, pH 5.5. Condensates were imaged using a LSM700 Airyscan confocal microscope (Zeiss) using a DIC20x 0.3 objective.

Nephelometry

WT, Q331K and R361S CTD variants were added to a 96-well, non-binding, flat-bottom, half-area microplate (Corning, USA; 10629151) at a concentration of 50 µM in 20 mM ammonium acetate, pH 5.5 with 0 mM NaCl or 150 mM NaCl added. Light scattering of 40 µL of each solution was then monitored using a Nephelostar plate reader (BMG Labtech, Ortenburg, Germany) using an excitation wavelength of 635 ± 10 nm, over 6 h at 25 °C. Data were blank corrected and three replicate measurements were conducted. Significance was assessed using an unpaired two-sided Welch's t-test on the blank corrected (linear) RNU values to account for unequal variances between conditions. Statistical analyses were performed in Python (SciPy). A threshold of $p < 0.05$ was considered significant. Where indicated in figures *** = p < 0.01.*

Coarse-grained molecular dynamics simulations

Coarse-grained implicit-solvent simulations of the TDP-43 CTD were performed in the in the OpenMM framework (version 8.1.1)[112] using the CALVADOS python package and the CALVADOS2 force field[91,113]. Simulations were performed for TDP-43 CTD WT, Q331K and R361S at low and high ionic strengths (20 and 170 mM). Unless stated otherwise simulation parameters used were kept as their default values for slab simulations in the software. Simulations were performed in a 15 x 15 x 150 nm box with 100 TDP-43 CTD molecules (pH 5.5). Following energy minimization, simulations were run at a temperature of 21 °C for a total of 10 µs each with coordinates being saved every 0.1 ns. The

simulation had a time step of 10 fs and a friction coefficient of 10 fs^{-1}. The first 0.1 μs of each simulation was considered to still be part of the equilibration time and therefore not included in the analysis. To reduce the total number of frames in the analysis, every 10th frame was included such that the analysis was performed on frame each 1 ns. The C_{sat} was calculated with inbuilt functions in the CALVADOS software, where the concentration is calculated for frames with z values greater than= ~50 nm and less than ~-50 nm (i.e., outside the dense phase). For each frame, the central chain was selected as the one closest to the mid-plane (z = 0 nm) of the protein-dense slab to avoid molecules near the slab interface, as is standard in analyses using the CALVADOS software package.

ACKNOWLEDGEMENTS

The authors acknowledge support from a Sir Henry Dale Fellowship (awarded to ANC) jointly funded by Wellcome and the Royal Society (Grant Number 220628/Z/20/Z). J.A.C acknowledges the support of the University of Leeds and the BBSRC (BB/Y00034X/1). ANC acknowledges support of a Royal Society research grant (RGS\R2\222357). P.A., C.C.C.C. and A.N.C. acknowledge funding from the BBSRC (BB/X003086/1). Funding from BBSRC enabled the purchase of mass spectrometry equipment (BB/M012573/1). The LSM700 Airyscan confocal microscope was funded by Wellcome (WT104918MA). The FEI Tecnai T12 TEM was funded by Wellcome (090932/Z/09/Z). We thank S. R. Ganji and G. Wildsmith for technical support and for maintaining the Biomolecular Mass Spectrometry Facility at the University of Leeds. We thank Professor Frank Sobott for fruitful discussions. Sheena Radford is thanked for critical reading of the manuscript. This work was undertaken in part on the Aire HPC system at the University of Leeds, UK.

AUTHOR CONTRIBUTIONS

Emily J. Byrd: conceptualization, methodology, validation, formal analysis, investigation, data curation, writing – original draft, visualization; Joel A. Crossley: formal analysis, investigation, data curation, visualization; Chalmers C. C. Chau: methodology, resources; Paolo Actis: conceptualization, methodology, validation, writing – review & editing, supervision, project administration; Antonio N. Calabrese: conceptualization, methodology, validation, writing – review & editing, supervision, project administration, funding acquisition.

REFERENCES

1. Suk TR, Rousseaux MWC (2020) The role of TDP-43 mislocalization in amyotrophic lateral sclerosis. Mol. Neurodegener. 15:45.

2. Khalfallah Y, Kuta R, Grasmuck C, Prat A, Durham HD, Vande Velde C (2018) TDP-43 regulation of stress granule dynamics in neurodegenerative disease-relevant cell types. Sci. Rep. 8:7551.

3. Gasset-Rosa F, Lu S, Yu H, Chen C, Melamed Z, Guo L, Shorter J, Da Cruz S, Cleveland DW (2019) Cytoplasmic TDP-43 DE-mixing independent of stress granules drives inhibition of nuclear import, loss of nuclear TDP-43, and cell death. Neuron 102:339-357.e7.

4. Lee Y-B, Scotter EL, Lee D-Y, Troakes C, Mitchell J, Rogelj B, Gallo J-M, Shaw CE (2021) Cytoplasmic TDP-43 is involved in cell fate during stress recovery. Hum. Mol. Genet. 31:166–175.

5. Banani SF, Lee HO, Hyman AA, Rosen MK (2017) Biomolecular condensates: organizers of cellular biochemistry. Nat. Rev. Mol. Cell Biol. 18:285–298.

6. Shin Y, Brangwynne CP (2017) Liquid phase condensation in cell physiology and disease. Science [Internet] 357. Available from: http://dx.doi.org/10.1126/science.aaf4382

7. Alberti S, Gladfelter A, Mittag T (2019) Considerations and challenges in studying liquid-liquid phase separation and biomolecular condensates. Cell 176:419–434.

8. Guseva S, Schnapka V, Adamski W, Maurin D, Ruigrok RWH, Salvi N, Blackledge M (2023) Liquid-Liquid Phase Separation Modifies the Dynamic Properties of Intrinsically Disordered Proteins. J. Am. Chem. Soc. 145:10548–10563.

9. Wang A, Conicella AE, Schmidt HB, Martin EW, Rhoads SN, Reeb AN, Nourse A, Ramirez Montero D, Ryan VH, Rohatgi R, et al. (2018) A single N-terminal phosphomimic disrupts TDP-43 polymerization, phase separation, and RNA splicing. EMBO J. [Internet] 37. Available from: http://dx.doi.org/10.15252/embj.201797452

10. de Oliveira GAP, Cordeiro Y, Silva JL, Vieira TCRG (2019) Liquid-liquid phase transitions and amyloid aggregation in proteins related to cancer and neurodegenerative diseases. Adv. Protein Chem. Struct. Biol. 118:289–331.

11. Cohen TJ, Lee VMY, Trojanowski JQ (2011) TDP-43 functions and pathogenic mechanisms implicated in TDP-43 proteinopathies. Trends Mol. Med. 17:659–667.

12. Kuo P-H, Chiang C-H, Wang Y-T, Doudeva LG, Yuan HS (2014) The crystal structure of TDP-43 RRM1-DNA complex reveals the specific recognition for UG- and TG-rich nucleic acids. Nucleic Acids Res. 42:4712–4722.

13. Prasad A, Bharathi V, Sivalingam V, Girdhar A, Patel BK (2019) Molecular Mechanisms of TDP-43 Misfolding and Pathology in Amyotrophic Lateral Sclerosis. Front. Mol. Neurosci. 12:25.

14. Zhang X, Vigers M, McCarty J, Rauch JN, Fredrickson GH, Wilson MZ, Shea J-E, Han S, Kosik KS (2020) The proline-rich domain promotes Tau liquid-liquid phase separation in cells. J. Cell Biol. [Internet] 219. Available from: http://dx.doi.org/10.1083/jcb.202006054

15. Shenoy J, Lends A, Berbon M, Bilal M, El Mammeri N, Bertoni M, Saad A, Morvan E, Grélard A, Lecomte S, et al. (2023) Structural polymorphism of the low-complexity C-terminal domain of TDP-43 amyloid aggregates revealed by solid-state NMR. Front Mol Biosci 10:1148302.

16. Conicella AE, Dignon GL, Zerze GH, Schmidt HB, D'Ordine AM, Kim YC, Rohatgi R, Ayala YM, Mittal J, Fawzi NL (2020) TDP-43 α-helical structure tunes liquid-liquid phase separation and function. Proc. Natl. Acad. Sci. U. S. A. 117:5883–5894.

17. Minshull TC, Byrd EJ, Olejnik M, Calabrese AN (2024) Hydrogen-deuterium exchange mass spectrometry reveals mechanistic insights into RNA oligonucleotide-mediated inhibition of TDP-43 aggregation. J. Am. Chem. Soc. 146:33626–33639.

18. Chien H-M, Lee C-C, Huang JJ-T (2021) The Different Faces of the TDP-43 Low-Complexity Domain: The Formation of Liquid Droplets and Amyloid Fibrils. Int. J. Mol. Sci. [Internet] 22. Available from: http://dx.doi.org/10.3390/ijms22158213

19. Igaz LM, Kwong LK, Chen-Plotkin A, Winton MJ, Unger TL, Xu Y, Neumann M, Trojanowski JQ, Lee VM-Y (2009) Expression of TDP-43 C-terminal fragments in vitro recapitulates pathological features of TDP-43 proteinopathies. J. Biol. Chem. 284:8516–8524.

20. Shenoy J, El Mammeri N, Dutour A, Berbon M, Saad A, Lends A, Morvan E, Grélard A, Lecomte S, Kauffmann B, et al. (2020) Structural dissection of amyloid aggregates of TDP-43 and its C-terminal fragments TDP-35 and TDP-16. FEBS J. 287:2449–2467.

21. Berning BA, Walker AK (2019) The pathobiology of TDP-43 C-terminal fragments in ALS and FTLD. Front. Neurosci. 13:335.

22. Cao Q, Boyer DR, Sawaya MR, Ge P, Eisenberg DS (2019) Cryo-EM structures of four polymorphic TDP-43 amyloid cores. Nat. Struct. Mol. Biol. 26:619–627.

23. Li Q, Babinchak WM, Surewicz WK (2021) Cryo-EM structure of amyloid fibrils formed by the entire low complexity domain of TDP-43. Nat. Commun. 12:1620.

24. Arseni D, Chen R, Murzin AG, Peak-Chew SY, Garringer HJ, Newell KL, Kametani F, Robinson AC, Vidal R, Ghetti B, et al. (2023) TDP-43 forms amyloid filaments with a distinct fold in type A FTLD-TDP. Nature 620:898–903.

25. Arseni D, Nonaka T, Jacobsen MH, Murzin AG, Cracco L, Peak-Chew SY, Garringer HJ, Kawakami I, Suzuki H, Onaya M, et al. (2024) Heteromeric amyloid filaments of ANXA11 and TDP-43 in FTLD-TDP Type C. bioRxiv [Internet]:2024.06.25.600403. Available from: https://www.biorxiv.org/content/10.1101/2024.06.25.600403v1

26. Sharma K, Stockert F, Shenoy J, Berbon M, Abdul-Shukkoor MB, Habenstein B, Loquet A, Schmidt M, Fändrich M (2024) Cryo-EM observation of the amyloid key structure of polymorphic TDP-43 amyloid fibrils. Nat. Commun. 15:486.

27. Arseni D, Hasegawa M, Murzin AG, Kametani F, Arai M, Yoshida M, Ryskeldi-Falcon B (2022) Structure of pathological TDP-43 filaments from ALS with FTLD. Nature 601:139–143.

28. Towle CA, Treadwell BV (1992) Identification of a novel mammalian annexin. cDNA cloning, sequence analysis, and ubiquitous expression of the annexin XI gene. J. Biol. Chem. 267:5416–5423.

29. Inukai Y, Nonaka T, Arai T, Yoshida M, Hashizume Y, Beach TG, Buratti E, Baralle FE, Akiyama H, Hisanaga S-I, et al. (2008) Abnormal phosphorylation of Ser409/410 of TDP-43 in FTLD-U and ALS. FEBS Lett. 582:2899–2904.

30. Neumann M, Sampathu DM, Kwong LK, Truax AC, Micsenyi MC, Chou TT, Bruce J, Schuck T, Grossman M, Clark CM, et al. (2006) Ubiquitinated TDP-43 in frontotemporal lobar degeneration and amyotrophic lateral sclerosis. Science 314:130–133.

31. Neumann M, Kwong LK, Lee EB, Kremmer E, Flatley A, Xu Y, Forman MS, Troost D, Kretzschmar HA, Trojanowski JQ, et al. (2009) Phosphorylation of S409/410 of TDP-43 is a consistent feature in all sporadic and familial forms of TDP-43 proteinopathies. Acta Neuropathol. 117:137–149.

32. Cohen TJ, Hwang AW, Restrepo CR, Yuan C-X, Trojanowski JQ, Lee VMY (2015) An acetylation switch controls TDP-43 function and aggregation propensity. Nat. Commun. 6:5845.

33. Cracco L, Doud EH, Hallinan GI, Garringer HJ, Jacobsen MH, Richardson RM, Buratti E, Vidal R, Ghetti B, Newell KL (2022) Distinguishing post-translational modifications in dominantly inherited frontotemporal dementias: FTLD-TDP Type A (GRN) vs Type B (C9orf72). Neuropathol. Appl. Neurobiol. 48:e12836.

34. Aikio M, Odeh HM, Wobst HJ, Lee BL, Chan Ú, Mauna JC, Mack KL, Class B, Ollerhead TA, Ford AF, et al. (2025) Opposing roles of p38α-mediated phosphorylation and PRMT1-mediated arginine methylation in driving TDP-43 proteinopathy. Cell Rep. 44:115205.

35. Saunders C, Rocha-Rangel P, Desai R, Quadri Z, Lui H, Hunt JB Jr, Liang H, Rogers C, Nash K, Tsoi PS, et al. (2025) Citrullination of TDP-43 is a key post-translation modification associated with structural and functional changes and progressive pathology in TDP-43 mouse models and human proteinopathies. bioRxiv [Internet]:2025.02.28.639952. Available from: https://www.biorxiv.org/content/10.1101/2025.02.28.639952v1.abstract

36. Kellett EA, Bademosi AT, Walker AK (2025) Molecular mechanisms and consequences of TDP-43 phosphorylation in neurodegeneration. Mol. Neurodegener. 20:53.

37. Conicella AE, Zerze GH, Mittal J, Fawzi NL (2016) ALS Mutations Disrupt Phase Separation Mediated by α-Helical Structure in the TDP-43 Low-Complexity C-Terminal Domain. Structure 24:1537–1549.

38. Chang Z, Deng J, Zhao W, Yang J (2020) Amyloid-like aggregation and fibril core determination of TDP-43 C-terminal domain. Biochem. Biophys. Res. Commun. 532:655–661.

39. Lin P-H, Wu G-W, Lin Y-H, Huang J-R, Jeng U-S, Liu W-M, Huang J-R (2024) TDP-43 amyloid fibril formation via phase separation-related and -unrelated pathways. ACS Chem. Neurosci. [Internet]. Available from: http://dx.doi.org/10.1021/acschemneuro.4c00503

40. Pesiridis GS, Lee VM-Y, Trojanowski JQ (2009) Mutations in TDP-43 link glycine-rich domain functions to amyotrophic lateral sclerosis. Hum. Mol. Genet. 18:R156-62.

41. Van Langenhove T, van der Zee J, Van Broeckhoven C (2012) The molecular basis of the frontotemporal lobar degeneration-amyotrophic lateral sclerosis spectrum. Ann. Med. 44:817–828.

42. Arnold ES, Ling S-C, Huelga SC, Lagier-Tourenne C, Polymenidou M, Ditsworth D, Kordasiewicz HB, McAlonis-Downes M, Platoshyn O, Parone PA, et al. (2013) ALS-linked TDP-43 mutations produce aberrant RNA splicing and adult-onset motor neuron disease without aggregation or loss of nuclear TDP-43. Proc. Natl. Acad. Sci. U. S. A. 110:E736-45.

780 43. Rizuan A, Shenoy J, Mohanty P, dos Passos PMS, Mercado Ortiz JF, Bai L, Viswanathan R,
781 Wang S-H, Johnson V, Mamede LD, et al. (2024) Structural details of helix-mediated TDP-43 C-
782 terminal domain multimerization. bioRxiv [Internet]:2024.07.05.602258. Available from:
783 https://www.biorxiv.org/content/10.1101/2024.07.05.602258v1.full

784 44. Babinchak WM, Haider R, Dumm BK, Sarkar P, Surewicz K, Choi J-K, Surewicz WK (2019) The
785 role of liquid-liquid phase separation in aggregation of the TDP-43 low-complexity domain. J. Biol.
786 Chem. 294:6306–6317.

787 45. Marklund EG, Degiacomi MT, Robinson CV, Baldwin AJ, Benesch JLP (2015) Collision cross
788 sections for structural proteomics. Structure 23:791–799.

789 46. Allison TM, Bechara C (2019) Structural mass spectrometry comes of age: new insight into
790 protein structure, function and interactions. Biochem. Soc. Trans. 47:317–327.

791 47. Stuchfield D, Barran P (2018) Unique insights to intrinsically disordered proteins provided by
792 ion mobility mass spectrometry. Curr. Opin. Chem. Biol. 42:177–185.

793 48. Beveridge R, Calabrese AN (2021) Structural Proteomics Methods to Interrogate the
794 Conformations and Dynamics of Intrinsically Disordered Proteins. Front Chem 9:603639.

795 49. Fenn JB (2003) Electrospray wings for molecular elephants (Nobel lecture). Angew. Chem.
796 Int. Ed Engl. 42:3871–3894.

797 50. Grandori R, Santambrogio C, Brocca S, Invernizzi G, Lotti M (2009) Electrospray-ionization
798 mass spectrometry as a tool for fast screening of protein structural properties. Biotechnol. J.
799 4:73–87.

800 51. Sterling HJ, Batchelor JD, Wemmer DE, Williams ER (2010) Effects of buffer loading for
801 electrospray ionization mass spectrometry of a noncovalent protein complex that requires high
802 concentrations of essential salts. J. Am. Soc. Mass Spectrom. 21:1045–1049.

803 52. Metwally H, McAllister RG, Konermann L (2015) Exploring the mechanism of salt-induced
804 signal suppression in protein electrospray mass spectrometry using experiments and molecular
805 dynamics simulations. Anal. Chem. 87:2434–2442.

806 53. Cassou CA, Williams ER (2014) Desalting protein ions in native mass spectrometry using
807 supercharging reagents. Analyst 139:4810–4819.

808 54. Susa AC, Xia Z, Williams ER (2017) Native Mass Spectrometry from Common Buffers with
809 Salts That Mimic the Extracellular Environment. Angew. Chem. Int. Ed Engl. 56:7912–7915.

810 55. Yuill EM, Sa N, Ray SJ, Hieftje GM, Baker LA (2013) Electrospray ionization from nanopipette
811 emitters with tip diameters of less than 100 nm. Anal. Chem. 85:8498–8502.

812 56. Susa AC, Lippens JL, Xia Z, Loo JA, Campuzano IDG, Williams ER (2018) Submicrometer
813 Emitter ESI Tips for Native Mass Spectrometry of Membrane Proteins in Ionic and Nonionic
814 Detergents. J. Am. Soc. Mass Spectrom. 29:203–206.

815 57. Panczyk EM, Gilbert JD, Jagdale GS, Stiving AQ, Baker LA, Wysocki VH (2020) Ion mobility and
816 surface collisions: Submicrometer capillaries can produce native-like protein complexes. Anal.
817 Chem. 92:2460–2467.

58. Drachman N, Lepoitevin M, Szapary H, Wiener B, Maulbetsch W, Stein D (2024) Nanopore ion sources deliver individual ions of amino acids and peptides directly into high vacuum. Nat. Commun. 15:7709.

59. Byrd EJ, Norgate EL, Crossley JA, Chau CC, Schiffrin B, Kulak A, Radford S, Actis P, Calabrese AN, Sobott F (2025) Buffer-dependent conformational dynamics of α-synuclein revealed by nanopipette electrospray ionisation ion mobility mass spectrometry. bioRxiv [Internet]:2025.08.19.671163. Available from: https://www.biorxiv.org/content/10.1101/2025.08.19.671163v1.abstract

60. Li H-R, Chen T-C, Hsiao C-L, Shi L, Chou C-Y, Huang J-R (2018) The physical forces mediating self-association and phase-separation in the C-terminal domain of TDP-43. Biochim. Biophys. Acta: Proteins Proteomics 1866:214–223.

61. Watkins JA, Alix JJP, Shaw PJ, Mead RJ (2021) Extensive phenotypic characterisation of a human TDP-43Q331K transgenic mouse model of amyotrophic lateral sclerosis (ALS). Sci. Rep. 11:16659.

62. Hardenberg M, Horvath A, Ambrus V, Fuxreiter M, Vendruscolo M (2020) Widespread occurrence of the droplet state of proteins in the human proteome. Proc. Natl. Acad. Sci. U. S. A. 117:33254–33262.

63. Vendruscolo M, Fuxreiter M (2022) Sequence determinants of the aggregation of proteins within condensates generated by liquid-liquid phase separation. J. Mol. Biol. 434:167201.

64. Hatos A, Tosatto SCE, Vendruscolo M, Fuxreiter M (2022) FuzDrop on AlphaFold: visualizing the sequence-dependent propensity of liquid-liquid phase separation and aggregation of proteins. Nucleic Acids Res. 50:W337–W344.

65. Ishida T, Kinoshita K (2007) PrDOS: prediction of disordered protein regions from amino acid sequence. Nucleic Acids Res. 35:W460-4.

66. Byrd EJ, Wilkinson M, Radford SE, Sobott F (2023) Taking Charge: Metal Ions Accelerate Amyloid Aggregation in Sequence Variants of α-Synuclein. J. Am. Soc. Mass Spectrom. 34:493–504.

67. Swain BC, Sarkis P, Ung V, Rousseau S, Fernandez L, Meltonyan A, Aho VE, Mercadante D, Mackereth CD, Aznauryan M (2024) Disordered regions of human eIF4B orchestrate a dynamic self-association landscape. Nat. Commun. 15:8766.

68. Xia Z, DeGrandchamp JB, Williams ER (2019) Native mass spectrometry beyond ammonium acetate: effects of nonvolatile salts on protein stability and structure. Analyst 144:2565–2573.

69. Rizuan A, Shenoy J, Mohanty P, Dos Passos PM, Mercado Ortiz JF, Bai L, Viswanathan R, Zaborowksy J, Wang S-H, Johnson V, et al. (2025) Structural details of helix-mediated multimerization of the conserved region of TDP-43 C-terminal domain. Nat. Commun. 16:10528.

70. Robb CG, Dao TP, Ujma J, Castañeda CA, Beveridge R (2023) Ion Mobility Mass Spectrometry Unveils Global Protein Conformations in Response to Conditions that Promote and Reverse Liquid-Liquid Phase Separation. J. Am. Chem. Soc. 145:12541–12549.

71. Osterholz H, Stevens A, Abramsson ML, Lama D, Brackmann K, Rising A, Elofsson A, Marklund EG, Deindl S, Leppert A, et al. (2025) Native mass spectrometry captures the conformational plasticity of proteins with low-complexity domains. JACS Au 5:281–290.

72. Byrd EJ, Rowlinson B, Crossley JA, Brockwell DJ, Ross JF, Radford SE, Sobott F (2025) Zn2+ binding shifts the conformational ensemble of α-synuclein monomers toward accelerated amyloid formation. J. Am. Chem. Soc. 147:36464–36477.

73. Stein A, Whitlock JP Jr, Bina M (1979) Acidic polypeptides can assemble both histones and chromatin in vitro at physiological ionic strength. Proc. Natl. Acad. Sci. U. S. A. 76:5000–5004.

74. Dang M, Lim L, Kang J, Song J (2021) ATP biphasically modulates LLPS of TDP-43 PLD by specifically binding arginine residues. Commun. Biol. 4:714.

75. Konermann L, Ahadi E, Rodriguez AD, Vahidi S (2013) Unraveling the mechanism of electrospray ionization. Anal. Chem. 85:2–9.

76. Pimlott DJD, Konermann L (2021) Using covalent modifications to distinguish protein electrospray mechanisms: Charged residue model (CRM) vs. chain ejection model (CEM). Int. J. Mass Spectrom. 469:116678.

77. Poudyal M, Patel K, Gadhe L, Sawner AS, Kadu P, Datta D, Mukherjee S, Ray S, Navalkar A, Maiti S, et al. (2023) Intermolecular interactions underlie protein/peptide phase separation irrespective of sequence and structure at crowded milieu. Nat. Commun. 14:6199.

78. Sun Y, Medina Cruz A, Hadley KC, Galant NJ, Law R, Vernon RM, Morris VK, Robertson J, Chakrabartty A (2019) Physiologically important electrolytes as regulators of TDP-43 aggregation and droplet-phase behavior. Biochemistry 58:590–607.

79. Sternke-Hoffmann R, Sun X, Menzel A, Dos Santos Pinto M, Venclovaitė U, Wördehoff M, Hoyer W, Zheng W, Luo J (2024) Phase Separation and Aggregation of α-Synuclein Diverge at Different Salt Conditions. bioRxiv [Internet]:2024.03.01.582895. Available from: https://www.biorxiv.org/content/10.1101/2024.03.01.582895v1.full

80. Duan C, Wang R (2024) A unified description of salt effects on the liquid-liquid phase separation of proteins. ACS Cent. Sci. 10:460–468.

81. Johnson BS, Snead D, Lee JJ, McCaffery JM, Shorter J, Gitler AD (2009) TDP-43 is intrinsically aggregation-prone, and amyotrophic lateral sclerosis-linked mutations accelerate aggregation and increase toxicity. J. Biol. Chem. 284:20329–20339.

82. Groenning M, Olsen L, van de Weert M, Flink JM, Frokjaer S, Jørgensen FS (2007) Study on the binding of Thioflavin T to beta-sheet-rich and non-beta-sheet cavities. J. Struct. Biol. 158:358–369.

83. Biancalana M, Makabe K, Koide A, Koide S (2009) Molecular mechanism of thioflavin-T binding to the surface of beta-rich peptide self-assemblies. J. Mol. Biol. 385:1052–1063.

84. Bieschke J, Zhang Q, Powers ET, Lerner RA, Kelly JW (2005) Oxidative metabolites accelerate Alzheimer's amyloidogenesis by a two-step mechanism, eliminating the requirement for nucleation. Biochemistry 44:4977–4983.

85. Maezawa I, Hong H-S, Liu R, Wu C-Y, Cheng RH, Kung M-P, Kung HF, Lam KS, Oddo S, Laferla FM, et al. (2008) Congo red and thioflavin-T analogs detect Abeta oligomers. J. Neurochem. 104:457–468.

86. Das T, Zaidi FK, Farag M, Ruff KM, Mahendran TS, Singh A, Gui X, Messing J, Taylor JP, Banerjee PR, et al. (2025) Tunable metastability of condensates reconciles their dual roles in amyloid fibril formation. Mol. Cell 85:2230-2245.e7.

87. Zheng T, Wake N, Weng S-L, Perdikari TM, Murthy AC, Mittal J, Fawzi NL (2025) Molecular insights into the effect of 1,6-hexanediol on FUS phase separation. EMBO J. 44:2725–2740.

88. Gadkari VV, Ramírez CR, Vallejo DD, Kurulugama RT, Fjeldsted JC, Ruotolo BT (2020) Enhanced Collision Induced Unfolding and Electron Capture Dissociation of Native-like Protein Ions. Anal. Chem. 92:15489–15496.

89. Borotto NB, Osho KE, Richards TK, Graham KA (2022) Collision-Induced Unfolding of Native-like Protein Ions Within a Trapped Ion Mobility Spectrometry Device. J. Am. Soc. Mass Spectrom. 33:83–89.

90. Cao F, von Bülow S, Tesei G, Lindorff-Larsen K (2024) A coarse-grained model for disordered and multi-domain proteins. Protein Sci. 33:e5172.

91. Tesei G, Lindorff-Larsen K (2022) Improved predictions of phase behaviour of intrinsically disordered proteins by tuning the interaction range. Open Res. Eur. 2:94.

92. Báez Bolivar EG, Bui DT, Kitova EN, Han L, Zheng RB, Luber EJ, Sayed SY, Mahal LK, Klassen JS (2021) Submicron emitters enable reliable quantification of weak protein-glycan interactions by ESI-MS. Anal. Chem. 93:4231–4239.

93. Jordan JS, Xia Z, Williams ER (2022) Tips on Making Tiny Tips: Secrets to Submicron Nanoelectrospray Emitters. J. Am. Soc. Mass Spectrom. 33:607–611.

94. Garaizar A, Sanchez-Burgos I, Collepardo-Guevara R, Espinosa JR (2020) Expansion of intrinsically disordered proteins increases the range of stability of liquid-liquid phase separation. Molecules 25:4705.

95. Martin EW, Holehouse AS, Peran I, Farag M, Incicco JJ, Bremer A, Grace CR, Soranno A, Pappu RV, Mittag T (2020) Valence and patterning of aromatic residues determine the phase behavior of prion-like domains. Science 367:694–699.

96. Choi J-M, Pappu RV (2020) The stickers and spacers framework for describing phase behavior of multivalent intrinsically disordered proteins. Biophys. J. 118:492a.

97. Chattaraj A, Shakhnovich EI (2025) Separation of sticker-spacer energetics governs the coalescence of metastable condensates. Biophys. J. 124:428–439.

98. Galvanetto N, Ivanović MT, Chowdhury A, Sottini A, Nüesch MF, Nettels D, Best RB, Schuler B (2023) Extreme dynamics in a biomolecular condensate. Nature 619:876–883.

99. Garcia-Cabau C, Salvatella X (2021) Regulation of biomolecular condensate dynamics by signaling. Curr. Opin. Cell Biol. 69:111–119.

100. Tibble RW, Gross JD (2023) A call to order: Examining structured domains in biomolecular condensates. J. Magn. Reson. 346:107318.

101. Lipiński WP, Visser BS, Robu I, Fakhree MAA, Lindhoud S, Claessens MMAE, Spruijt E (2022) Biomolecular condensates can both accelerate and suppress aggregation of α-synuclein. Sci. Adv. 8:eabq6495.

936 102. Zhang S, Lim CM, Occhetta M, Vendruscolo M (2024) AlphaFold2-based prediction of the
937 co-condensation propensity of proteins. Proc. Natl. Acad. Sci. U. S. A. 121:e2315005121.

938 103. Li Y, Gu J, Wang C, Hu J, Zhang S, Liu C, Zhang S, Fang Y, Li D (2022) Hsp70 exhibits a liquid-
939 liquid phase separation ability and chaperones condensed FUS against amyloid aggregation.
940 iScience 25:104356.

941 104. Gu J, Liu Z, Zhang S, Li Y, Xia W, Wang C, Xiang H, Liu Z, Tan L, Fang Y, et al. (2020) Hsp40
942 proteins phase separate to chaperone the assembly and maintenance of membraneless
943 organelles. Proc. Natl. Acad. Sci. U. S. A. 117:31123–31133.

944 105. Pakravan D, Michiels E, Bratek-Skicki A, De Decker M, Van Lindt J, Alsteens D, Derclaye S,
945 Van Damme P, Schymkowitz J, Rousseau F, et al. (2021) Liquid-Liquid Phase Separation
946 Enhances TDP-43 LCD Aggregation but Delays Seeded Aggregation. Biomolecules [Internet] 11.
947 Available from: http://dx.doi.org/10.3390/biom11040548

948 106. Bush MF, Hall Z, Giles K, Hoyes J, Robinson CV, Ruotolo BT (2010) Collision Cross Sections
949 of Proteins and Their Complexes: A Calibration Framework and Database for Gas-Phase
950 Structural Biology. Anal. Chem. 82:9557–9565.

951 107. Christofi E, Barran P (2023) Ion mobility mass spectrometry (IM-MS) for structural biology:
952 Insights gained by measuring mass, charge, and collision cross section. Chem. Rev. 123:2902–
953 2949.

954 108. Cheung See Kit M, Cropley TC, Bleiholder C, Chouinard CD, Sobott F, Webb IK (2023) The
955 role of solvation on the conformational landscape of α-synuclein. Analyst 149:125–136.

956 109. Jeacock K, Chappard A, Gallagher KJ, Mackay CL, Kilgour DPA, Horrocks MH, Kunath T,
957 Clarke DJ (2023) Determining the Location of the α-Synuclein Dimer Interface Using Native Top-
958 Down Fragmentation and Isotope Depletion-Mass Spectrometry. J. Am. Soc. Mass Spectrom.
959 34:847–856.

960 110. Moons R, Konijnenberg A, Mensch C, Van Elzen R, Johannessen C, Maudsley S, Lambeir A-
961 M, Sobott F (2020) Metal ions shape α-synuclein. Sci. Rep. 10:16293.

962 111. Bush MF, Campuzano IDG, Robinson CV (2012) Ion mobility mass spectrometry of peptide
963 ions: effects of drift gas and calibration strategies. Anal. Chem. 84:7124–7130.

964 112. Eastman P, Swails J, Chodera JD, McGibbon RT, Zhao Y, Beauchamp KA, Wang L-P,
965 Simmonett AC, Harrigan MP, Stern CD, et al. (2017) OpenMM 7: Rapid development of high
966 performance algorithms for molecular dynamics. PLoS Comput. Biol. 13:e1005659.

967 113. Tesei G, Schulze TK, Crehuet R, Lindorff-Larsen K (2021) Accurate model of liquid-liquid
968 phase behavior of intrinsically disordered proteins from optimization of single-chain properties.
969 Proc. Natl. Acad. Sci. U. S. A. 118:e2111696118.